Faculteit Wetenschappen

Departement Fysica

Optimization of electron tomography for the three dimensional study of nanoparticle assemblies

Eva Bladt
Promotor: Prof. Dr. Sara Bals

Academiejaar 2012-2013

Proefschrift ter verkrijging van de graad van Master in de Fysica

Acknowledgement

I firstly want to thank my promotor, Prof. Dr. Sara Bals, for her unconditional and constant support during my master thesis. Starting from my bachelor thesis, her enthusiasm, passion and drive encouraged me to work hard. I am grateful to Sara for introducing me to the 'world' of electron microscopy. I sincerly hope there will be more years of teamwork to come!

Besides my promotor, I also want to thank my supervisors, Dr. Hamed Heidari Mezerji and Dr. Frederic Leroux. Hamed almost became family because of his intensive and ongoing support and guidance. Thank you, Hamed, for our endless discussions, all the hours at the microscope, and teaching me so much! Frederic was always there to help me throughout the thesis and I could always count on his encouragment. I will never forget his supporting presence while taking a manual tilt series of 281 images! Also, many thanks to Bart Goris, Thomas Atlantzis and Mert Kurttepeli for sharing their knowledge.

I owe a big thanks to my friends, in particular Benjamin, Christophe and Sam for helping me forget about the thesis, for a very short time, on relaxing sundays.

Finally, I want to thank my family. My sister for helping me with Photoshop, my brother for our physics discussions and especially my mother for learning me to work hard and for always standing by my side.

Thank you for your confidence,

Eva

Abstract

Door de toenemende interesse in assemblies van nanodeeltjes, is karakterisatie een belangrijke stap om de relatie tussen de structuur en de eigenschappen van deze assemblies te begrijpen. Conventionele transmissie-elektronenmicroscopie (TEM) is niet voldoende om een materiaal in 3 dimensies te karakteriseren, omdat deze methode enkel 2-dimensionale (2D) beelden levert van een 3D object. Daarom wordt elektronentomografie gebruikt, een methode om een 3-dimensionale (3D) reconstructie te maken uitgaande van 2D projecties. Hiervoor wordt een reeks beelden opgenomen van hetzelfde gebied, telkens onder een licht verschillende hoek. Aan de hand van een algoritme, worden deze beelden omgezet in een 3D reconstructie van het originele object. In dit werk, wordt gezocht naar het geoptimaliseerde elektronentomografie experiment om assemblies van nanodeeltjes te karakteriseren.
Wanneer enkele druppels van de suspensie worden gedeponeerd op een TEM grid, zullen de structuren inzakken op het grid. Deze inzakking is te wijten aan de verdamping van het oplosmiddel, waarin de nano-assemblies zich bevinden. Er moet dus een andere techniek gevonden worden zodat de structuren hun initiële structuur behouden. In dit opzicht, wordt een oorspronkelijk biologische techniek gebruikt, *plunge-freezing*. Hierbij worden de samples omgeven door een dunne ijslaag en moeten daardoor onderzocht worden bij vloeibare stikstof temperaturen. Buiten deze moeilijkheid, zijn er ook beperkingen op de beeldvormingstechniek bij het nemen van de reeks projectie beelden. Daarom wordt een derde behandelingsmethode toegepast, *freeze-drying*, waarbij de samples met dunne ijslaag weer worden opgewarmd. Deze opwarming introduceert een overgang van vaste fase naar de gasvormige fase, zonder eerst over te gaan naar de vloeibare fase. Het onderzoeken van deze samples heeft geen beperkingen en de optimale beeldvormingsmethode kan gebruikt worden. Uiteindelijk wordt ook nog gezocht naar het optimale reconstructie algoritme om de projectie beelden om te zetten in een 3D structuur.

Contents

Chapter 1

Introduction

1.1 Nano-assemblies

Self assembled nanostructures are the result of the organization of discrete components, here nanoparticles, due to specific interactions between the mutual components and the interaction with their environment. In order to assemble these nanoscopic components into a larger configuration, a profound knowledge and understanding of the interparticle interactions (magnetic, electrostatic, van der Waals, molecular) is required. This knowledge yields the possibility to create systems in which parameters such as the size of the individual particles and the configuration of the three dimensional (3D) stacking can be tuned. In order to develop such tunable self-assemblies for technological applications and to ensure efficient production, a high level of direction and control is necessary *(Grzelczak, 2010)*. Nanoscaled assemblies are promising to deliver solutions for applications concerning biomedical applications *(Tam, 2010)*, drug delivery *(Kim, 2008, Sánchez-Iglesias, 2012)*, medical diagnostics *(Besenius 2012, Liang 2011)*, sensors *(Li, 2010, Alvarez-Puebla, 2012)* and materials with unique, specific properties *(Guerrero-Martínez, 2011)*.

1.1.1 Investigation techniques

Controlled synthesis of nanoparticles has been extensively studied because it is of key importance for a better design of nanomaterials, such as nano-assemblies, with tailored properties. To improve the control of the design on the particles, a better understanding of the growth process is necessary. Transmission electron microscopy is an ideal tool to investigate nanoparticles and their assemblies. For instance, in situ transmission electron microscopy techniques have been used to monitor the growth of colloidal platinum nanocrystals *(Zheng, 2009, Yuk, 2012)* and of bismuth nanoparticles in liquid cells *(Xin, 2012)*. Transmission electron microscopy (TEM) techniques are also often used to examine the final state of a nano-assembly *(Martínez,*

2010). Since new advances in the field of materials growth enable the synthesis of 3D nano-assemblies, the characterization by transmission electron microscopy should be optimized as well.

1.1.2 Outline of experimental research

Characterization is a crucial step towards understanding the relation between the structure and properties of nano-assemblies. To obtain a 3D characterization, we cannot use conventional transmission electron microscopy (TEM) since this method only provides two dimensional (2D) images of a 3D object. Therefore, electron tomography is required to obtain a 3D characterization. Electron tomography has become a standard technique in the 3D characterization of nanomaterials *(Midgley & Bals, 2013)*. In this work, the main goal is to characterize nanoparticle assemblies in the most optimal electron tomography experiment.
In the rest of this chapter, we will discuss the different forms of electron microscopy imaging, and afterwards electron tomography is explained. In chapter 2, we search for the optimized technique for image acquisition of the nano-assemblies and in chapter 3 the algorithms to yield a 3D reconstruction are discussed. Finally, in chapter 4, we investigate the quality of the 3D reconstructions.

1.2 Conventional TEM imaging

1.2.1 History

Transmission electron microscopes are developed to acquire images with a spatial resolution, which cannot be obtained using a light microscope. The resolution of an optical instrument is determined by the ability to distinquish separate points of an object that are located at a small angular distance. With our eyes this distance is up to $0.1 - 0.2\ mm$. If we are interested in smaller details, a microscope is required. The resolution of a light microscope is limited by the wavelength of the radiation source, which is approximately given by the Rayleigh criterion:

$$\delta = \frac{0.61\lambda}{\mu sin(\beta)}$$

with λ the wavelength of the radiation, μ the refractive index of the viewing medium and β the semi-angle of collection of the magnifying lens. For green light in the middle of the visible spectrum, λ is about $550\ nm$, so the resolution of a visible light microscope is about $300\ nm$. If we want to visualize details below this limit, we need to use a type of radiation with a shorter wavelength. Since the wavelength of accelerated electrons is much shorter than the wavelength of visible light, electrons

are suitable. The wavelength of electrons is approximately given by the de Broglie's equation:

$$\lambda = \frac{1.22}{E^{1/2}}$$

with E the energy of the accelerated electrons in electron volts (eV) and λ in nanometer (nm). For electrons accelerated to 100 keV, λ is approximately 4 pm. However, it should be noted that the resolution of a TEM does not equal 4 pm. The resolution of a TEM is not only limited by the wavelength of the electrons, but also by the lenses in the microscope.
The first idea of an electron microscope was proposed by Knoll and Ruska in 1932, and was commercialised by Siemens and Halske in Germany 1939. Ernst Ruska received the Noble Prize in Physics for his contribution to electron optics in 1986.

1.2.2 The transmission electron microscope

The motivation to switch from visible light to electrons was explained in section 1.2.1, but in general the basic principles of a TEM are similar to those of a light microscope. Apart from the different illumination source, another important difference is the use of electro-magnetic lenses in a TEM instead of glass lenses. From top to bottom, a TEM consists of an illumination system with an electron gun and a condensor lens system, the stage of the specimen and the imaging system with different lenses. There are two kinds of commonly used electron sources in a TEM, a thermionic source and a field-emission source. A thermionic source produces electrons when it is heated and the latter when a large electric potential is applied between the source and an anode. After the electron production, the electrons are transfered to the specimen. The electrons are generated with a specific energy, typically in the order of several hundred keV. The accelerated electrons then pass through a condensor lense in order to create a parallel beam. This beam interacts with the specimen and using the lenses in the imaging system, an enlarged image is formed.

1.2.3 Electron specimen interaction

The electrons interact with the Coulombic potential distribution within the specimen, when they penetrate the sample. The electrons transmitted through the specimen are divided into two groups, unscattered electrons that suffer no angular deviation and electrons scattered at certain angles. The pathway of the electrons through the specimen can either involve an energy transfer or a negligible energy transfer, the scattering is referred to as inelastic or elastic respectively. After a first scattering, it is possible that the electrons will scatter again, either elastically or inelastically. The probability of the second scattering event increases for thicker samples. Single scattering is the simplest scattering process, therefore it is important to use TEM

samples, as thin as possible. If the sample is thin enough, all the scattering events can be approximated as single scattering.
The elastically scattered electrons, which are low angle scattered electrons, are used for conventional TEM imaging, diffraction pattern imaging and high resolution TEM (HR-TEM) imaging.

1.2.4 Contrast formation mechanisms

When an electron wave transverses the specimen, both the amplitude and the phase of the electron wave can change. In most cases, both types of contrast contribute to the image formation, however the selection of one dominating contrast formation mechanism is suggested.
When discussing the contrast of an image, we have to be careful not to address the intensity of the image as the contrast. The contrast is defined as the difference in intensity between an area rich in contrast and a background area:

$$C = \frac{I - I_{background}}{I_{background}}$$

Intensity refers to the density of electrons hitting the screen or the detector. Contrast can be weak or strong and intensity can be light or dark, which is illustrated in figure 1.1.

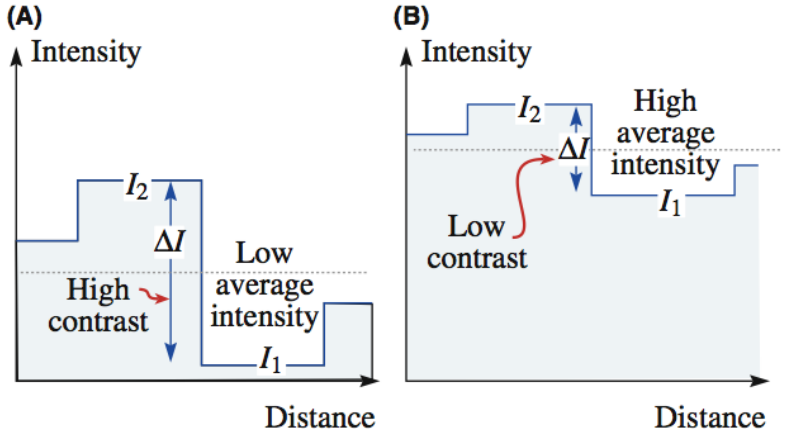

Figure 1.1: Schematic overview of the difference between contrast and intensity. The intensity profiles show different intensity levels (I_1 and I_2) and the difference (ΔI), which defines the contrast *(Williams, 1996)*.

When the incident beam with uniform electron intensity passes through the specimen, it results in a non-uniform intensity at the image plane due to these variations.

The variable electron intensity is translated into contrast of the image. In the following sections we will discuss different imaging techniques that are important for electron tomography in more detail.

BF-TEM: Amplitude contrast

The amplitude contrast can be distinguished into two types, mass-thickness contrast and diffraction contrast. In order to obtain interpretable amplitude contrast, either the direct beam or a diffracted beam has to be selected. In a TEM, this selection is performed by using an objective aperture. If we do not use an objective aperture, the contrast will be lower because we use many beams for the image formation. Selecting the direct beam or scattered beams, results in creating bright field (BF) or dark field (DF) images respectively. The ray diagrams of both imaging modes are illustrated in figure 1.2.

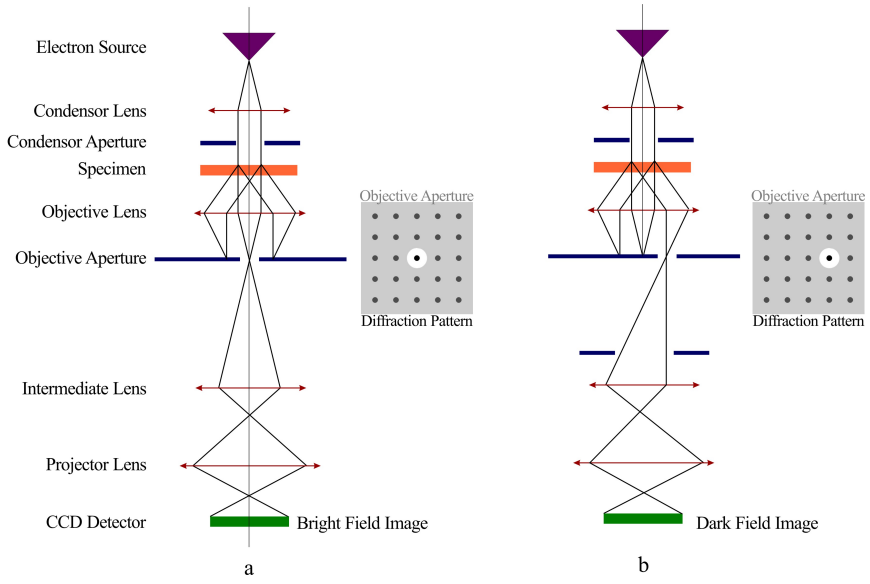

Figure 1.2: Schematic overview of (a) bright-field and (b) dark-field imaging *(Heidari Mezerji, 2012).*

The **mass-thickness contrast** is determined by the variations of mass and thickness of the specimen. In amorphous structures, heavy atoms scatter the electrons to higher angles and thereby it is possible that these electrons do not pass the aperture of the central beam. Lighter atoms scatter the electrons to smaller angles and they are more likely to pass the aperture. Considering a homogeneous thickness for the specimen, in this manner, the heavier atoms will appear with darker contrast than the lighter atoms. This is called mass contrast. A BF-TEM image is also formed

by thickness contrast. Thicker areas of the specimen will have less intensity because more electrons are scattered in that area.
Diffraction contrast is a special form of amplitude contrast where the scattering occurs at specific angles. In crystalline structures, the incident parallel electron beam is diffracted by the crystal lattice of the specimen, which is the result of scattering of the electrons when interacting with the specimen. The scattering of the electrons within the crystal lattice of the specimen generates a phase difference. The phase difference can result in constructive or destructive interference, which appears as a diffraction pattern in the back focal plane of the objective lens. If the beam satisfies Bragg's law, constructive interference will take place. These reflections are given by Bragg's law:

$$sin(\theta) = \frac{n\lambda}{2d}$$

where θ is the Bragg angle, n is an integer, λ is the wavelength of the incident beam and d is the crystallographic inter-planar distance. The intensity of the diffracted beam is dependent on the thickness of the specimen and the reflections depend on the angle of the incident beam according to Bragg's law. Because of this dependence, the contrast in the real space image differs according to the orientation of the specimen in reference to the incident electron beam.
In dark-field imaging, the diffracted beams are used for the image formation where an objective aperture is selected which blocks the central beam and passes one or more diffracted beams. These diffracted beams contain a lot of information about the structure of the specimen.
The bright field (BF) technique uses the primary undeflected beam to contribute to the projection image by the addition of an aperture. The objective aperture is placed in the back focal plane of the objective lens. The size of this aperture controls the collection angle *(Williams, 2009)*. The contrast of a BF-TEM image is predominantly determined by mass-thickness contrast. The bright field technique is schematically presented in figure 1.2a.

HAADF-STEM: Z-contrast

Scanning transmission electron microscopy (STEM) is an imaging mode where a focussed electron beam scans over the specimen. To scan the region of interest, the current of the scanning coils are adapted, where the scanning takes place line by line. In order to collect the electrons, to be used for the image formation, the location of the detector needs to be adjusted. The selection of the imaging electrons is based on their scattering angle (figure 1.3). The two most common applications of STEM imaging are bright field STEM (BF-STEM) and dark field STEM (DF-STEM). When we want to apply BF-STEM, the detector collects the central electrons. In annular DF-STEM (ADF-STEM), an annular detector is used to collect the electrons scattered to a large angle between 10 and 50 mrad. When the electrons scattered to high

angles (> 50 mrad) are collected, the imaging mode is called high angle ADF-STEM (HAADF-STEM). These electrons can be considered as Rutherford scattered particles, therefore the high-angle scattering is associated with the interaction close to the nucleus of the atoms. For Rutherford scattering the interaction is dependent of the atomic number (Z) and applies that the signal is proportional to Z^n with $1.6 < n < 2$ *(Kirkland, 1987, Pennycook, 1992)*.

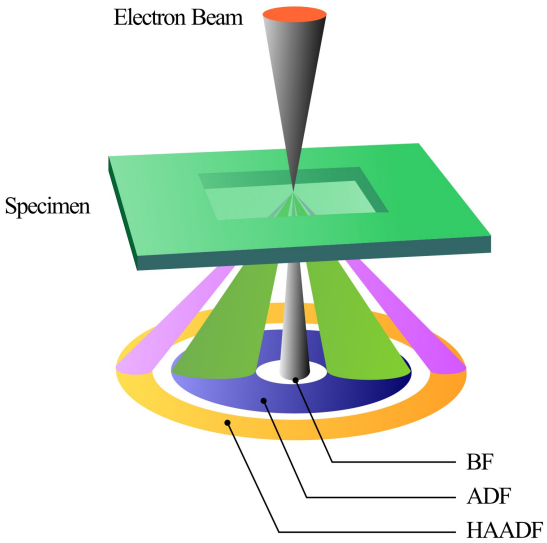

Figure 1.3: Schematic drawing of different detectors, collecting the electrons at different angles. The BF detecor collects the central, unscattered beam. The ADF detector and HAADF detector collect the electrons scattered to larger angles, respectively between 10 and 50 mrad and > 50 mrad *(Heidari Mezerji, 2012)*.

1.3 Electron tomography

A (S)TEM image is only a 2D projection of a 3D structure. By applying electron tomography, one is able to obtain the 3D structure of the object based on a series of 2D projection images. Essentially, electron tomography consists of four main steps, which are schematically shown in figure 1.4. In the first step, a series of tilt images is acquired from the same region of interest over a tilt range in angular increments of typically 1 or 2 degrees. The obtained tilt series of images is aligned to a common tilt axis in order to eliminate relative shifts and rotations between the successive images. A reconstruction is calculated using a mathematical algorithm applied to the aligned series of images. In the last step, a quantification of the tomogram is carried out for

further analysis.
Before these different steps are explained in detail, some basic principles of tomographic imaging are explained.

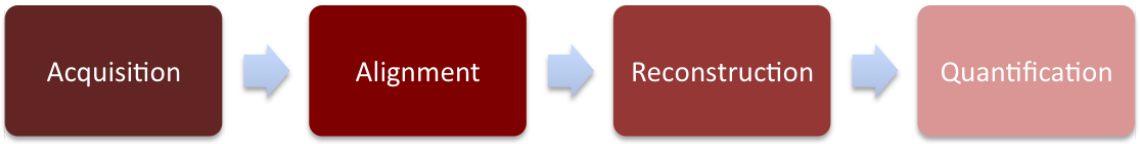

Figure 1.4: A schematic overview of the successive steps in an electron tomography experiment towards a 3D reconstruction.

1.3.1 Theory behind tomography

The Radon transform

Radon, an Austrian mathematician, was the first who outlined the mathematical principles behind the tomography technique in 1917 *(Radon, 1917)*. The Radon transform defines the relationship between the real space object and its projections, or line integrals, through the object. Line integrals are defined as an integral of a certain property of an object along a line. The Radon transform in 2D is the integral transform consisting of an integral of a function along straight lines.
The projection, and thus a line integral, of a defined object $f(x, y)$ is given by

$$P_\theta(t) = \int_{L(\theta,t)} f(x,y)ds \tag{1.1}$$

The line integral is defined on a line with an inclination with angle θ with respect to the y-axis and at a distance t from the origin, thereby expression 1.1 can be written as

$$P_\theta(t) = \int_{-\infty}^{\infty}\int_{-\infty}^{\infty} f(x,y)\delta(x\cos\theta + y\sin\theta - t)dxdy \tag{1.2}$$

The equation of a line through the object $f(x, y)$ is

$$t = x\cos\theta + y\sin\theta \tag{1.3}$$

thereby we will only find a result for the Radon transform, $P_\theta(t)$, along those lines because $\delta(x\cos\theta + y\sin\theta - t)$ is then equal to 1.
The Radon transformation converts the coordinates of the data into the 'Radon

space' (t, θ), where t is the line perpendicular to the projection direction and θ is the angle of the projection. The Radon transform is often called a 'sinogram', because the transformation of a Dirac delta function is a sinusoidal line.
A single projection of the object $f(x, y)$ yields a line at constant θ in Radon space. In order to use the Radon transform for tomography, a series of projections at different angles needs to be acquired. Increasing the number of projections, will lead to a better sampling of the Radon space and will thereby yield a more accurate reconstruction of the original object.

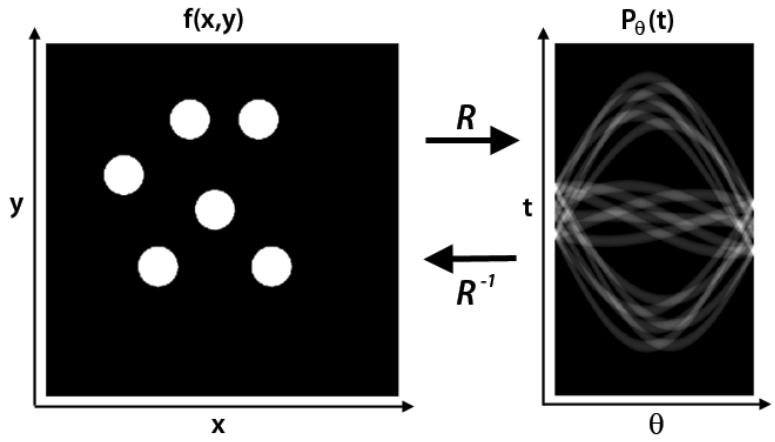

Figure 1.5: An example of an object, $f(x, y)$, and its sinogram, $P_\theta(t)$.

Fourier slice theorem

The reconstruction from projections is based on a relationship between the projections in real space and the Fourier space. The Fourier slice theorem describes this relationship and states that a projection of an object at a certain angle corresponds to a central section through the Fourier transform of that object. Therefore, to obtain the reconstruction, one needs to calculate the inverse Fourier transform.
The derivation of the Fourier slice theorem will be given in this section, providing that the one dimensional (1D) Fourier transform of a projection is equal to a slice of the two dimensional (2D) Fourier transform of the object. The derivation is based on a 2D object however it can be extended to higher dimensions as well. First, the 2D Fourier transform of an object $f(x, y)$ is defined as

$$F(u, v) = \int_{-\infty}^{\infty} \int_{-\infty}^{\infty} f(x, y) \mathrm{e}^{-i2\pi(ux+vy)} dxdy \tag{1.4}$$

where $u = q\cos\theta$ and $v = q\sin\theta$. The 1D Fourier transform of a parallel projection $P_\theta(t)$ is given by

$$S_\theta(q) = \int_{-\infty}^{\infty} P_\theta(t)\mathrm{e}^{-i2\pi qt}dt \tag{1.5}$$

We will proceed the derivation from the simplest case for the theorem, by considering the projection at angle $\theta = 0$, which leads to the transform of the object along the line $v = 0$ in the frequency domain, with

$$F(u,0) = \int_{-\infty}^{\infty}\int_{-\infty}^{\infty} f(x,y)\mathrm{e}^{-i2\pi ux}dxdy \tag{1.6}$$

Because the phase factor does not depend on y any longer, we can rewrite this integral as

$$F(u,0) = \int_{-\infty}^{\infty}\left[\int_{-\infty}^{\infty} f(x,y)dy\right]\mathrm{e}^{-i2\pi ux}dx \tag{1.7}$$

where the term inside the brackets corresponds to a projection along the y-axis

$$P_\theta(x) = \int_{-\infty}^{\infty} f(x,y)dy \tag{1.8}$$

Combining equation 1.7 and 1.8 gives the following equation

$$F(u,0) = \int_{-\infty}^{\infty} P_\theta(x)\mathrm{e}^{-i2\pi ux}dx \tag{1.9}$$

In equation 1.9, the right-hand side is the 1D Fourier transform of the projection $P_{\theta=0}$, which points out the relationship between a parallel projection and the 2D Fourier transform of the object. It is evident that this relationship applies for the projections at all angles, and not only for $\theta = 0$. We conclude that the 1D Fourier transform of the projection of an object yields a section through the origin in Fourier space, which is perpendicular to the direction of the projection.
In order to reconstruct the object by taking the 2D inverse Fourier transformation, the Fourier space needs to be sampled over the full range of frequencies. However it is not possible to sample over the full range, because an infinite number of projections cannot be obtained in practice. Since the images are acquired at discrete angles, there are regular gaps in Fourier space, which will not result in a perfect reconstruction of the object. The error will increase in the calculation of higher frequency components because of undersampling of Fourier space at these higher frequencies. The central

part of Fourier space is more closely sampled (illustrated in figure 1.6), the sampling density is proportional to the distance from the origin. The oversampled central part will result in a blurred reconstructed object.

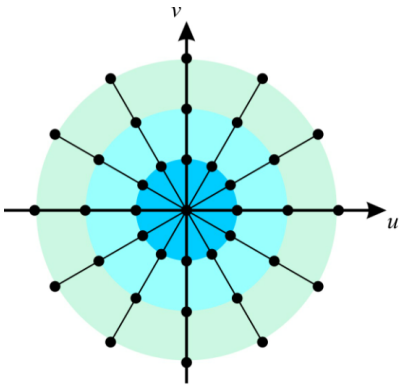

Figure 1.6: Sampling of the frequency domain, with a more closely sampled region around the origin *(Heidari Mezerji, 2012)*.

In order to remove this blurring in the reconstruction, different weighting filters can be multiplied to the reconstruction in Fourier space. The most common filter is the ramp filter $|f|$, where f represents the frequency. This ramp filter enhances the higher spatial frequencies and minimizes the lower spatial frequencies, i.e. corrects for uneven sampling. This reconstruction approach is called the weighted back projection (WBP). It is also possible to solve the reconstruction problem iteratively, which is further explained in section 1.3.2.

1.3.2 Tomography in practice

The projection requirement for electron tomography

A transmitted signal needs to fulfill several assumptions to be suitable for tomographic reconstruction *(Hawkes, 1992)*. The most important assumption is that some sort of projection through the structure should be obtained. *Formally, the projection requirement states that "this 'projection' need not to be a sum or integral through the structure of some physical property; in principle a monotonically varying function would be acceptable" (Midgley, 2003).*

Imaging techniques for tomography

The HAADF-STEM technique is highly recommended when investigating crystalline specimens, instead of the BF-TEM technique. In general, for most crystalline specimens, the BF contrast will be formed predominantly by diffraction contrast (figure 1.7). Diffraction contrast depends on the orientation of the specimen. Therefore,

this contrast formation mechanism will have no monotonic relationship with the amount of material where the beam passed through and in this way the projection requirement is not fulfilled. The image contrast of the HAADF-STEM technique, which is called Z-contrast, is due to the Z-value and the thickness of the sample; the diffraction contrast is almost completely eliminated. The intensity of HAADF-STEM images varies monotonically with the specimen composition (Z-value) and the specimen thickness [1] and thereby, the projection requirement is satisfied *(Midgley, 2003)*.

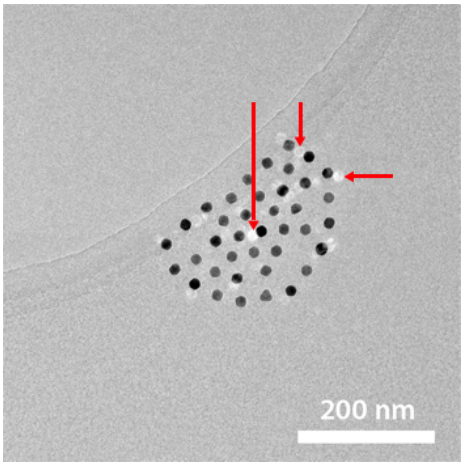

Figure 1.7: BF-TEM image of a cluster of Au nanoparticles. Several nanoparticles produce displaced diffracted beams (arrowed) because of their crystallographic orientation relative to the electron beam.

Single axis tilt acquisition

Single axis tilt acquisition is the most general acquisition scheme. It is based on tilting the specimen around the eucentric axis of the microscope stage with constant angular tilt increment over a large tilt range. For specimen with a slab geometry we have to consider that the thickness of the specimen increases with the tilt angle, illustrated in figure 1.8. In order to correct for this thickness variation throughout the tilt series, the Saxton step increment can be used. The Saxton scheme uses smaller step size at higher tilt angles to compensate the uneven sampling of the object. The tilt angles for the Saxton scheme are given by

$$\alpha_{n+1} = \alpha_n + \sin^{-1}(\sin\alpha_0 \cos\alpha_0) \tag{1.10}$$

where α_0 is the initial angular increment.

[1] This linear relation between the intensity of a HAADF-STEM image and specimen thickness yields only up to a certain thickness *(Pennycook, 2000)*.

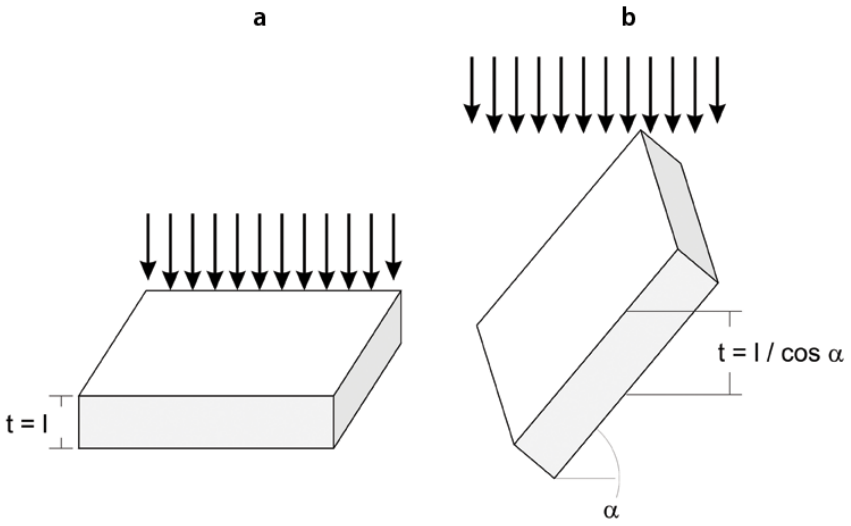

Figure 1.8: Schematic drawing of a slab geometry (a) at zero tilt and (b) at α tilt, with t the effective thickness and l the layer thickness. When tilting the slab over an angle α, the effective thickness, where the electrons pass through, increases with a factor $\frac{1}{\cos\alpha}$.

To collect all the information to create an accurate 3D reconstruction, the sample needs to be tilted ideally over 180° in the microscope. In figure 1.9, the acquisition of a tilt series for electron tomography is shown. Because of the limited spacing between the pole pieces of the objective lens of the microscope and the tilt limit of the microscope goniometer (illustrated in figure 1.10), it is not always possible to cover the full range. The limited angular range leads to missing projections at the high tilt angles and results in a 'missing wedge' of information in Fourier space and thereby induces artifacts in the 3D reconstruction. The 'missing wedge' is schematically shown in figure 1.11.

Alignment

When acquiring the images at the different tilt angles, the specimen is tracked into the field of view at each angle, which results in possible local shifts between the different images. In order to obtain a 3D reconstruction of the tilt series, these local shifts need to be compensated for. In reality, the local shifts can not be completely removed but should be minimized. To compensate for these shifts, we search for the common tilt axis of all images. The alignment procedure in general is done either by fiducial marker tracking or by cross-correlation.
The fiducial marker tracking alignment requires that markers are added to the sample. The alignment is then done by measuring the coordinates of the fiducial markers through the entire tilt series. Typically Au nanoparticles are used as fiducial marker.

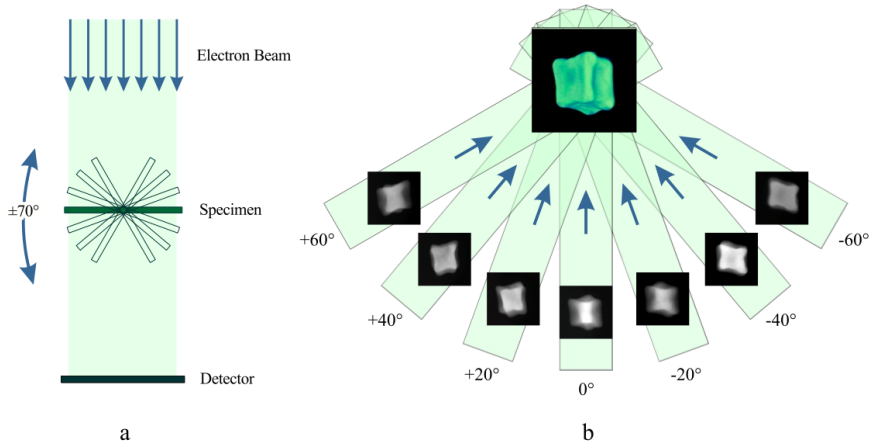

Figure 1.9: (a) Single axis tilt acquisition geometry. The specimen is projected by the microscope while tilting over an angular range in certain tilt increments. (b) A HAADF-STEM series of a truncated cubic Au nanoparticle *(Heidari Mezerji, 2012)*.

When using cross-correlation (figure 1.12) for the alignment, there is no need for markers. The method is based on calculating the cross-correlation between two successive projection images. The cross-correlation image is formed by multiplying the Fourier transform of the first projection with the complex conjugate of the Fourier transform of the second projection. The actual cross-correlation image is the invers Fourier transform of this product. The position of the maximum intensity in the cross-correlation presents the relative shift between the two projections. The correlation will not coincide completely because the two projections are acquired at different tilt angles, therefore the peak determination is done iteratively and can not be solved exactly. To simplify the determination of the peak position of the cross-correlation image, a band pass filter is often used. The band pass filter is applied on both projections before the cross-correlation image is obtained, which improves the quality of the peak determination. Here, the alignment was based on cross-correlation, executed by the program Inspect3D.

Reconstruction

The purpose of the tomographic reconstruction is to obtain the 3D structure of the specimen from the aligned tilt series. There are several approaches for the reconstruction.
As mentioned in section 1.3.1, the 3D structure can be reconstructed by an analytical method, such as WBP. These analytical methods are based on the central slice theorem. Back projection is based on evenly distributing the intensity in each projection image over computed backprojection rays. This back projecting process

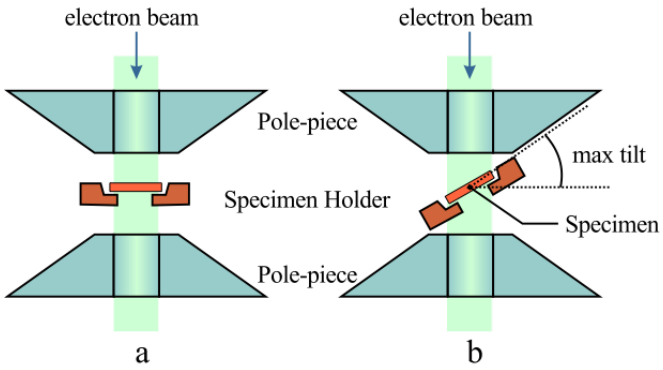

Figure 1.10: (a) Schematic overview of the specimen in the specimen holder with respect to the pole pieces of the objective lens at zero tilt. (b) Illustration of the maximum achievable tilt *(Heidari Mezerji, 2012)*.

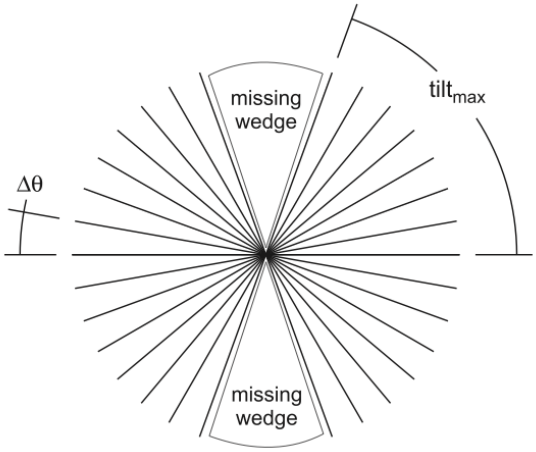

Figure 1.11: The missing wedge of information for a single tilt acquisition geometry is indicated *(Heidari Mezerji, 2012)*.

is repeated for all the projection images, which results in intersecting rays at certain positions. The intersection reinforces the intensity at points where mass is present in the orginal structure. The resulting reconstruction yields blurring in real space due to the uneven sampling of the spatial frequencies in Fourier space, which is solved by applying a weighted filter.
The reconstruction can also be done by an iterative technique, which formulates the reconstruction problem as a large set of linear equations:

$$A\mathbf{x} = \mathbf{b}$$

where A is the projection matrix, $\mathbf{x}$ the original object and $\mathbf{b}$ all the projection data. The solution to the reconstruction problem is found based on an iterative method.

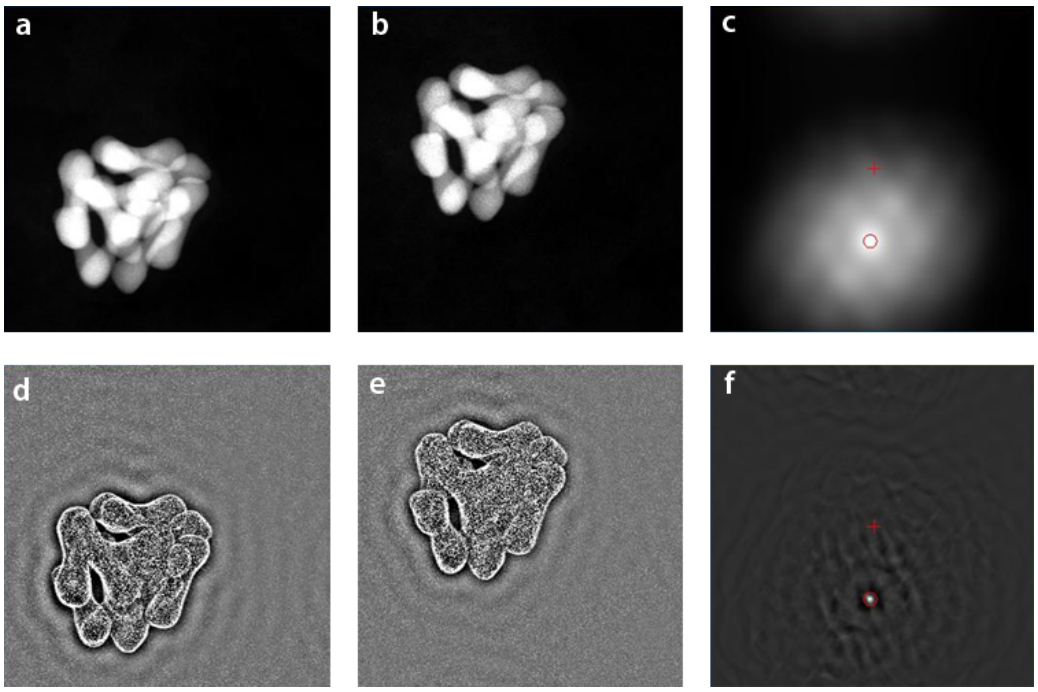

Figure 1.12: Example of the cross-correlation procedure to determine the relative shift between two images. (a,b) Two successive images of a Au dumbbell-shaped nanoparticle assembly using HAADF-STEM. (c) The cross-correlation between images a and b, showing a high intensity peak at (-12.72, 227.80) pixels from the image center, which corresponds to the shift between the two images. (d,e) Images a and b after applying a band-pass and morphological filter. (f) The cross-correlation between d and e, which shows an improvement in sharpness of the high intensity peak. The filtered cross-correlation shows a shift of (-12.46, 227.78).

These iterative reconstruction algorithms are developed to improve the quality of the reconstuction in comparison to the quality of the reconstruction when using weighted back projection. The latter quality is far from perfect because of the limited sampling in Fourier space. The improvement of the iterative algorithms is based on the fact that each projection is a perfect reference of the object.
Nowadays, the most popular iterative technique is the simultaneous iterative reconstruction technique (SIRT). SIRT is based on reprojecting the current reconstruction and comparing the reprojections to the original projections. By taking the difference projection, a difference reconstruction can be obtained to correct the previous reconstruction. This procedure is performed iteratively until an adequate solution is reached (figure 1.13). A criterion for the optimal number of iterations was proposed by Heidari Mezerji et al *(Heidari Mezeji, 2011)*.
Recently a new iterative technique was implemented for electron tomography, which

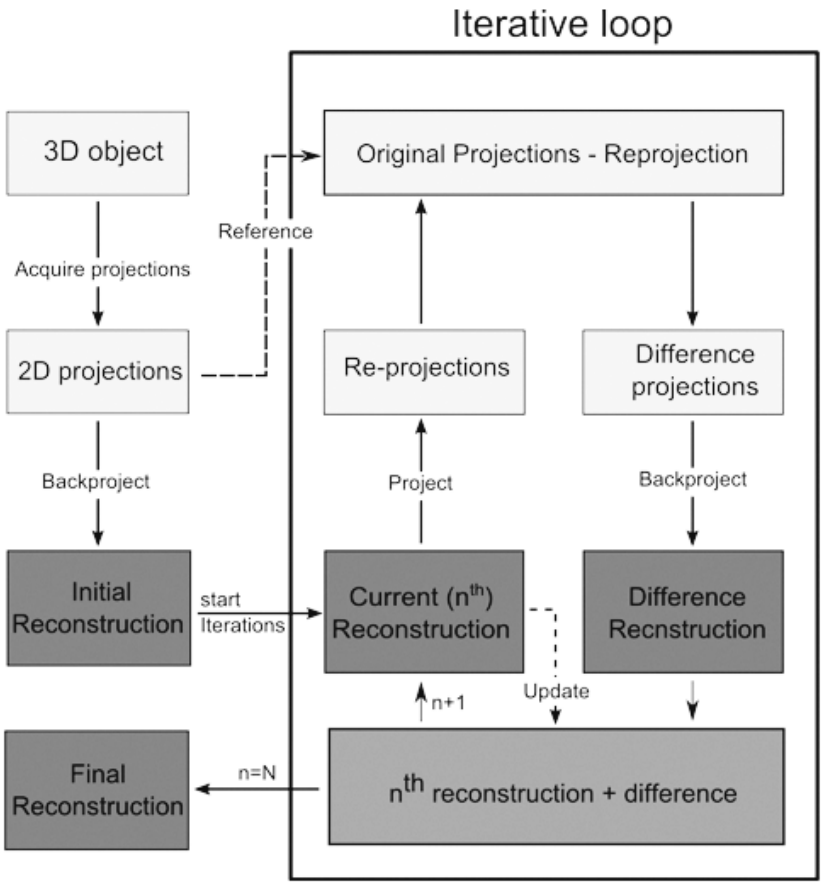

Figure 1.13: Schematic overview of the SIRT algorithm.

is known as total variation minimization (TVM) *(Goris, 2012)*. In this work the TVM algorithm is also applied on the tilt series. Additionaly, the metal artifact reduction (MAR) algorithm was applied on the BF-TEM series. In section 3.2 and 3.1, the procedure of the algorithms is explained.

1.4 Electron tomography of nano-assemblies

The preparation method of the TEM sample for electron tomography studies of nano-assemblies is of crucial importance when investigating the 3D arrangement of nanoparticles in a nano-assembly. The methodology for TEM specimen preparation needs to maintain the initial structure of the nano-assemblies, as they are present in the solution. The most straightforward sample preparation method is air drying

the sample solution onto a carbon coated TEM grid (figure 1.14), which is a very straightforward and quick technique:

- First the carbon coated support grids are made hydrophilic which allows the solution to spread easily over the whole surface of the grid.
- The specimens are prepared by applying one or two droplets of suspension of Au nanoparticles on the copper grid.
- In order to accelerate the drying process, the grid is afterwards placed under infrared light.

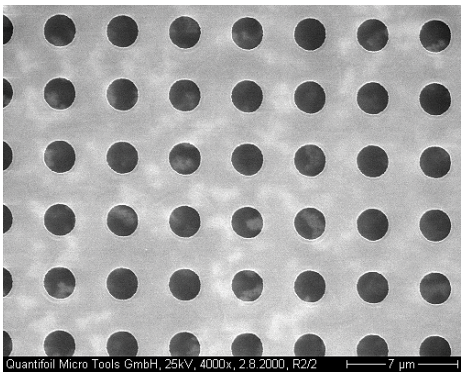

Figure 1.14: Image of a quantifoil carbon film, which is a perforated support foil with a precisely predefined hole size, shape and arrangement.

Initially, the Au nanoparticle clusters have a spherical 3D structure. Air-drying the specimen onto a support grid, leads to collapsed structures upon solvent evaporation and polymer desintegration. Figure 1.15 shows a BF-TEM and a HAADF-STEM image of a collapsed cluster of Au nanospheres. In figure 1.16, we present a visualization of a tomographic reconstruction of such a collapsed structure. Both an orthoslice and a 3D rendering are shown.

This confirms that air drying the specimen results in flat assemblies. Therefore, we try to optimize the sample preparation in order to maintain the initial structure of the nano-assembly.

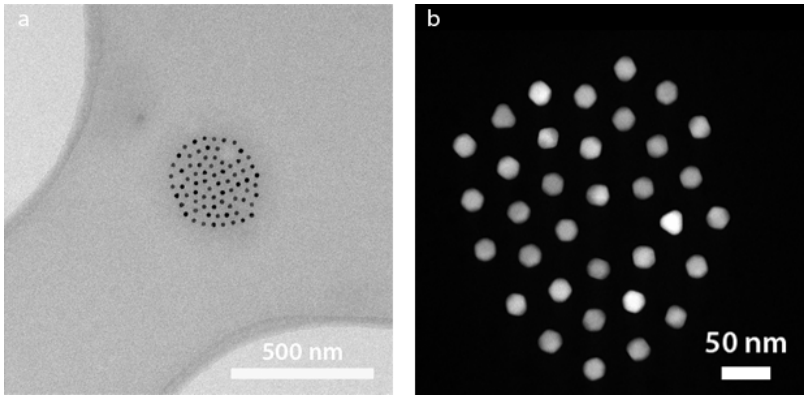

Figure 1.15: (a) BF-TEM image and (b) HAADF-STEM image of a flat nano-assembly in the air dried sample.

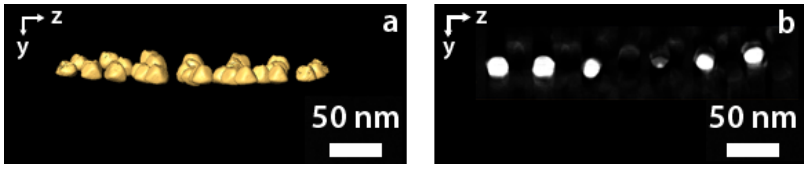

Figure 1.16: (a) 3D reconstruction of the assembly in figure 1.15b and (b) an orthoslice through the 3D reconstructed volume, corresponding to the YZ plane. The tilt series was acquired over a tilt range of $\pm 72^{\circ}$ with an increment of 2°.

Chapter 2

Optimization of the acquisition for electron tomography

2.1 Materials

In this work, we investigated nano-assemblies of Au nanospheres and nanodumbbells embedded in a polymeric matrix. Self-assembly of nanoparticles within the framework of bottom-up approach, which requires a precise organization of nanosized building blocks in three dimensions, is crucial for the development of new functional materials. Especially the use of metallic particles is attractive, since they are promising for applications in biosensing *(Rosi, 2005)* or energy conversion *(Linic, 2011)*. The investigation of nanodumbbells is of even higher interest, because the aim of assembly formation is gradually shifting towards the use of anisotropic nanoparticle building blocks *(Glotzer, 2007, Nie, 2010, Guerrero-Martínez, 2012)*. By increasing the anisotropy of Au nanoparticles, specific plasmonic and optical properties can be achieved. Therefore, directional interactions will play an important role in mimicking the creation of colloidal molecules. Anisotropic nanoparticles will facilitate directional clustering via steric constraints imposed by shape, thereby restricting clustering along certain directions. The study of asssemblies of anisotropic, dumbbell-like plasmonic particles into cross-like structures is promising to understand complex plasmonic phenomena. As an example, such clusters of Au nanoparticles may find applications in metamaterials with negative index of refraction *(Grzelczak, 2012)*. In general, dumbbell-shaped nanoparticles present several interesting features, including their axial symmetry and varying thickness from the thicker tips to the thinner central part. The varying thickness should result in characteristic properties compared to regular nanodumbbells. However, achieving cross-like nanoparticle assemblies is far from trivial.

The 3D stacking of the nanoparticles is primarily depending on parameters such as the size of the Au nanoparticles and the molecular weight of the polymer. Tuning

these parameters will lead to assemblies varying in size and morphology.

- **Preparation of assemblies of Au nanospheres** *(Sánchez-Iglesias, 2012)*
  - The nanospheres are stabilized by embedding the particles in a polymeric matrix, hydrophobic polystyrene.
  - The polymer-stabilized nanoparticles are dispersed in a tetrahydrofuran (THF) solution (figure 2.1a).
  - After addition of water, the spherical nanoparticles form clusters (figure 2.1b).
  - The size of the clusters is controlled by quenching, i.e. by addition of a bi-functional linear diblock copolymer (polystyrene-poly acrylic acid). The copolymer ensures the stability of the clusters in water, while the core remains hydrophobic (figure 2.1c).

- **Preparation of assemblies of Au nanodumbbells** *(Grzelczak, 2012)*
  - The nanodumbbells are embedded in the same polymeric matrix as the one used to stabilize the nanospheres.
  - The polymer coated nanodumbbells are dispersed in a THF/ dimethylformamide (DMF) solution (figure 2.2a).
  - Upon addition of water, the nanodumbbells undergo a side-to-side clustering. In the presence of water, the self-assembly of nanodumbbells is governed by poor solubility of the polystyrene, initially promoting the formation of side-to-side dimers and eventually larger clusters are aggregated (figure 2.2b).
  - By adding a polymeric surfactant to the solution, the nanodumbbells will cross-link. The copolymer molecules have the tendency to encapsulate the Au nanorod clusters and form a uniform organic shell, which induces the cross-linking (figure 2.2c).

Figure 2.3 shows HAADF-STEM images of clusters of (a) polystyrene-coated Au nanoparticles (specimen 1) and (b) Au nanodumbbells (specimen 2) found in the air dried sample. In figure 2.4, several cross-like dimers are visualized. The aim of this research is to characterize these assemblies in three dimensions. In the introduction, it is explained that air drying the samples, will lead to alterted, collapsed nano-assemblies, which is clearly visualized in figure 2.3. Therefore, we need to optimize the prepation method of the TEM samples, in order to maintain the initial structure.

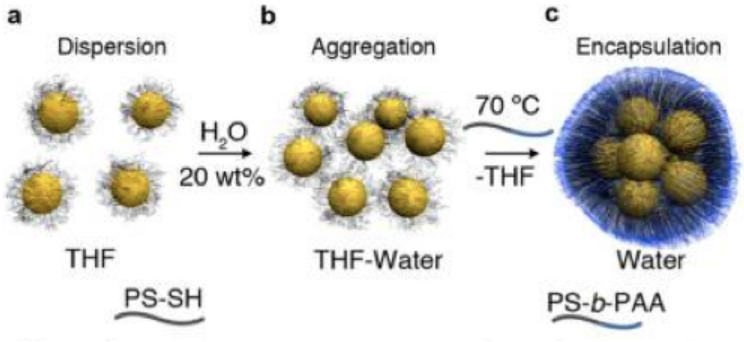

Figure 2.1: Schematic overview of the fabrication of a three-dimensional assembly of polystyrene-coated Au nanoparticles (specimen 1). (a) Polystyrene-coated Au nanoparticles in THF. (b) The continuous clustering of the nanoparticles is induced by addition of water to the THF solution. (c) Quenching the cluster growth by diblock copolymer and further thermal treatment which leads to the formation of Au nanoparticle clusters. ***(Sánchez-Iglesias, 2012)***

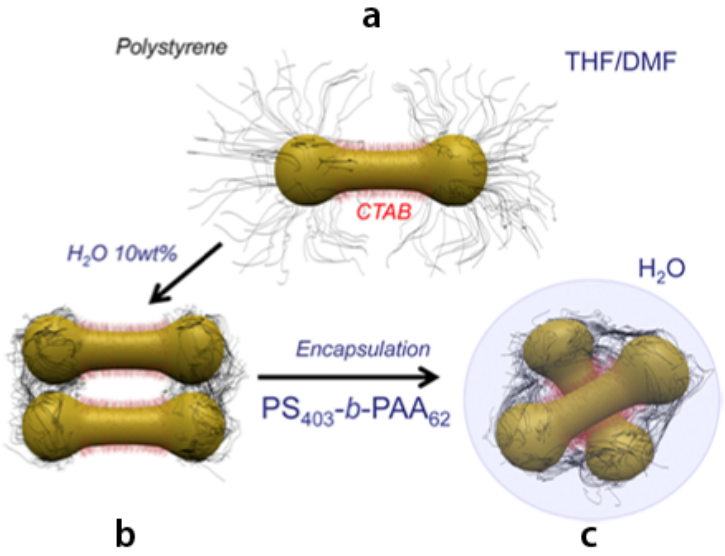

Figure 2.2: Schematic overview of the fabrication of the cross-like Au nanorod assembly (specimen 2). (a) The nanodumbbells are coated with polystyrene in a THF/DMF solution. (b) Subsequently, they undergo gradual dimer clustering upon addition of water to the solution. (c) Finally, the encapsulation of the clusters, incorporated by copolymer molecules, leads to the formation of cross-like assemblies. ***(Grzelczak, 2012)***

2.2 Optimization of sample preparation

Cryogenic electron microscopy (EM) studies the sample at cryogenic temperatures. It allows the visualization of a specimen in its native or liquid state. The basic goal is to

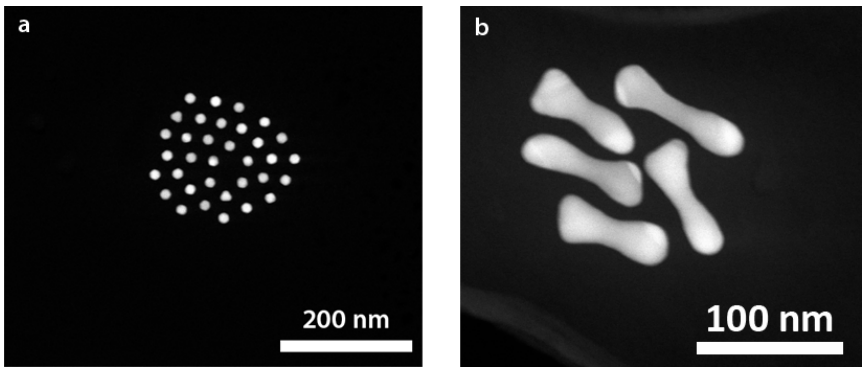

Figure 2.3: HAADF-STEM images of (a) specimen 1 and (b) specimen 2 in the air dried sample.

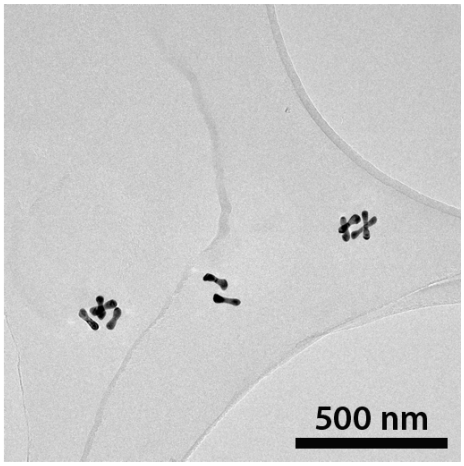

Figure 2.4: BF-TEM image of specimen 2 with several cross-like nanodumbbell dimers.

use cryofixation to rapidly freeze a sample as not to destroy its aqueous environment. This avoids artifacts or redistribution of elements within the specimen and maintains the structure as close as possible to the native state. Simply, depositing some droplets of the nano-assembly solution on a TEM grid results in a collapsed arrangement of the nanoparticles, which does not reflect the initial structure of the assembly. In order to avoid this redistribution of the nanoparticles, we applied cryogenic electron tomography on material science samples. So far, cryogenic EM has mostly been used for the investigation of biological samples. It can therefore be expected that the experimental parameters will need to be optimized during the investigation of the nano-assemblies.

2.2.1 Cryogenic tomography

Conventional TEM studies typically require high vacuum conditions. To fulfill these conditions, conventional drying and chemical fixation are employed which may lead to deformations of the sample inner structure. It is more favorable to study biological samples, and soft matter in general, in a more native state, because studying these samples in a dried state generally does not reflect their native hydrated stucture and configuration.
The preparation methods necessary for cryo-TEM do not require chemical fixation nor dehydration. The samples are plunge-frozen into a cryogen (e.g. liquid ethane), which results in embedding the sample in a thin layer of vitreous ice. The vitreous water does not contain any crystals and is transparent to the electron beam. The sample is then studied at liquid nitrogen temperature to maintain the vitrified state. When investigating vitrified samples, the sensitivity of the specimen to the electron beam presents the limiting factor in cryotomography. Both the vitrified ice matrix and the encapsulated nanostructures can be sensitive to electron beam damage. To avoid unnecessary irradiation of the specimen, the images are acquired at a low-dose mode. In this mode, the total amount of allowable dose is only used for the actual acquisition of the images of the tilt series. The total allowable dose needs to be distributed over the number of images of the tilt series. We have to take in mind that the thickness of the vitreous ice layer increases with $\cos^{-1}\alpha$ at higher tilt angles α. Therefore it is necessary to use more dose at higher tilt angles to maintain the same signal-to-noise ratio (SNR) in the different images. To apply more dose, the exposure time is increased at higher tilt angles. During the image acquisition, the focus for each image has to be optimized. Focusing also implies irradiation of the beam-sensitive specimen. In the low-dose mode, this focusing step is carried out at some distance from the field of interest. In this manner, we can fully use the dose for exposing the specimen when acquiring the images of the tilt series.
Here, we propose to vitrify the nano-assemblies, in order to maintain the initial 3D arrangement of the individual nanoparticles and therefore, the low dose TEM imaging mode is used to acquire the projections of the vitrified samples.

2.2.2 Plunge-freezing

Several preparation techniques are available to obtain a thin amorphous layer of ice in which the specimen is embedded. The choice of which technique to use is mainly dictated by the dimensions of the specimen. A commercial automated plunge-freezer is commonly used for biological and industrial suspensions with sizes smaller than 1 micrometer. This technique recently became available at the University of Antwerp. Since the plunge-freezing technique has only been used for the preparation of biological samples, it is challenging to apply the plunge-freezing on material science samples. Therefore, the technique needs to optimized, which is required for the

study of nano-assemblies. In this way, we try to combine the optimal preparation technique for biological samples with material science. The protocol that was found to yield the best results is explained below.
Prior to the vitrification process, a support grid, held in place by a tweezer, is attached to a plunger. A carbon support grid has the tendency to be hydrophobic. Therefore before the suspension can be placed onto the grid, it needs to be made hydrophilic which allows the solution to spread easily. To realize this hydrophilization, an oxygen plasma treatment, using a glow discharge, is applied. It is advisable to use support grids with circular holes. The applied sample solution will have a slightly biconcave surface inside the holes of the grid. Thereby, the solvent film will be thinner in the center of the holes in comparison to the thickness at the edges. After preprocessing the grid, we strart the actual plunge-freezing procedure *(Friedrich, 2010)*.

- A small droplet, typically 3 μl of suspension is applied onto the support film of the grid (figure 2.5a).

- The excess fluid is carefully blotted away by pressing two filter papers against the grid. The blot time and force can be adjusted to obtain a thin layer of water having a thickness of approximately 100 nm. This blotting process reduces the solution on the grid about 5000 times in volume (figure 2.5b). The purpose of the blotting process is to yield a high surface-to-volume ratio which ensures a fast heat exchange through the solution.

- After a predetermined time interval, the blotted grid is frozen by fast immersion into the cryogen.

    ◇ This freezing process must be fast enough ($< 3\ ms$) to prevent the formation of crystalline ice. Although liquid nitrogen is sufficiently cold, its heat capacity is low and hence, rapid cooling is prevented. Ethane, on the other hand, has a higher heat capacity than liquid nitrogen. It is the most efficient cryogen when cooled close to its freezing point (-188°C) using liquid nitrogen. To accomplish this, a small recipient of ethane is placed inside a larger nitrogen reservoir.

    ◇ Once the ethane in the vial is completely frozen, it needs to be slightly melted.

    ◇ Next, the grid is immersed into the ethane at high speed (figure 2.5c).

    ◇ It is also critical to maintain a higher relative humidity in the immediate area of the sample grid to prevent evaporation. Therefore, it is necessary to work close to 100% humidity. It is of the outmost importance that the vitrification process is performed in a temperature- and humidity-controlled environment. When the specimens are prepared in

an uncontrolled atmosfere, evaporation and heat transfer will take place which introduces artifacts *(Bellare, 1988, Vos, 2008)*.
Here, the polymer-coated Au nanoparticles are dispersed in a THF/water mixture. In order to prepare the sample properly, the environment inside the blotting chamber should contain THF. However, the humidifier is not designed to contain organic solvents. To solve this problem, we propose that a small cup with THF is placed inside the blotting chamber, creating a THF atmosphere.

◇ A good vitrification results in an evenly spread specimen embedded in a thin layer of vitreous ice.

- Finally, the frozen grid can be transferred to a storage box in liquid nitrogen for later use in the microscope. A schematic overview of the plunge-freezing technique is presented in figure 2.5.

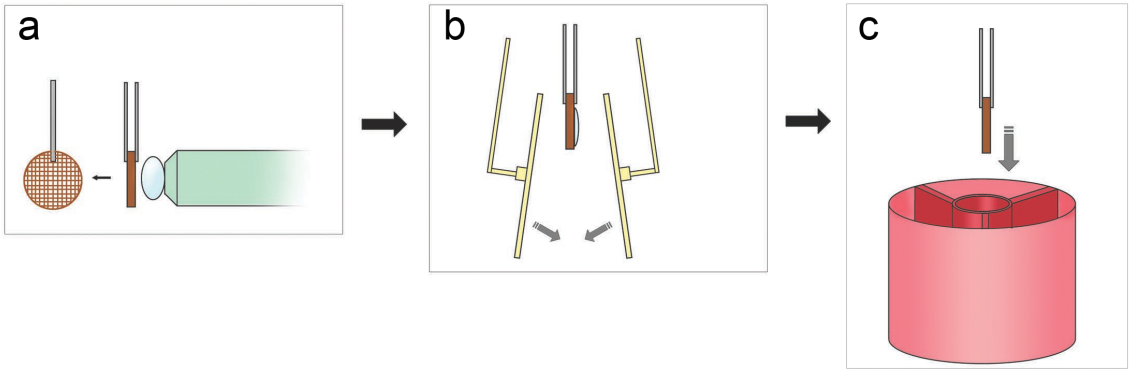

Figure 2.5: Schematic overview of the plunge-freezing process. (a) Using a pipette, a droplet of solution ($\pm$3-5 μl) is placed on a hydrophilic grid. (b) During the blotting process, the excess of solution is removed. (c) After blotting, the grid is plunged in liquid ethane. The ethane container is placed in a larger container filled with liquid nitrogen.

The drawback of the plunge-freezing process is that after cooling the solution in the cryogen, the sample needs to be kept cool at liquid nitrogen temperature at all times. To realize this condition, the transfer from the Vitrobot to the cryospecimen holder is done in a specialized workstation, which is cooled with liquid nitrogen. The cryospecimen holder is also designed to keep the sample in the vitrified state by conducting the cooling of the Dewar flask to the sample.

Parameters that affect the quality of the vitrified samples

Several parameters that will affect the quality and reproducibility of the vitrified specimen are listed below.

Support film

Using a support film with the appropriate surface properties is crucial to obtain reproducible results. Freshly produced carbon films are hydrophilic and become hydrophobic over time as contaminants from the atmosphere adsorb to the carbon surface. A plasma system is used to remove these hydrocarbon contaminants by means of a controlled glow discharge. As a result, the hydrophilic character is restored and the applied suspension spreads out evenly across the surface of the support film.

Automation, blotting and environmental parameters

In order to yield reproducible results, the sample preparation is performed using the Vitrobot (FEI Company, the Netherlands). The Vitrobot ensures a temperature and humidity controlled blotting chamber, which is essential to guarantee the reproducibility and quality of the vitrification process. The quality of the vitrified sample is mainly determined by the thickness of the ice layer and absence of cubic crystalline ice. The thickness of the ice can be affected by several parameters such as the cooling rate of the aqueous solution during the vitrification process, the blotting process and the humidity inside the blotting chamber. The blotting process can be adapted by an appropriate choice of blot time and blot offset. The blot time indicates how long the grid is blotted. The blot offset parameter controls the position of the grid between the two blotting pads. Adjusting this parameter affects the pressure of the filter paper on the grid and hence the thickness of the water film. The humidity of the blotting chamber is set to 100% humidity, to avoid evaporation and heat transfer which induces artifacts *(Iancu, 2006)*.

2.2.3 Cryotransfer

Procedure

After the sample is plunge-frozen, it first needs to be transfered to the holder and then to the microscope. In this section, the procedure of mounting the sample into the cryospecimen holder is visually explained. In the next section more information about the cooling system of the cryospecimen holder is given. Figure 2.6 shows the cryospecimen holder and the workstation.

First, the cryospecimen holder needs to be inserted into the workstation. Subsequently, we have to pre-cool the holder and the workstation with liquid nitrogen (figure 2.7a and 2.7b). After several minutes the temperature will be stabilized. When the temperature is stabilized, the actual mounting of the sample can start.

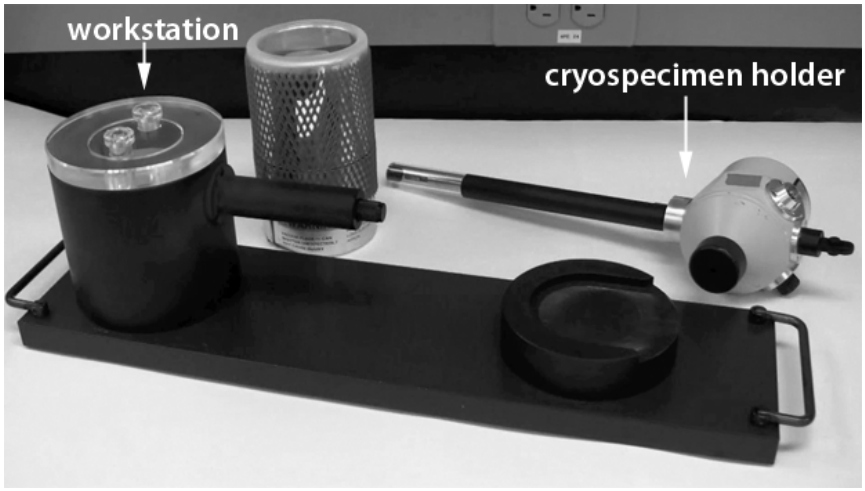

Figure 2.6: After plunge-freezing the sample, the cryospecimen holder and the workstation are necessary to mount the sample.

The cryo gridbox, which stores the plunge-frozen samples, can be inserted into the workstation. Next, the cryo shutter of the holder is opened, which gains access to the mounting position of the grid. Now, the sample can be mounted into the cryospecimen holder (figure 2.7c) and is secured with the clipring (figure 2.7d).
Only the cryo shutter needs to be closed and then the sample is ready to be transfered into the airlock of the electron microscope. Throughout the whole procedure, one needs to be careful to keep the liquid nitrogen level in the workstation high enough at all times.

Cryospecimen holder

As mentioned before, after sample preparation of the vitrified samples, the samples have to be kept cooled at all times. When the samples experience heating, devitrification is possible. Therefore the sample needs to be cooled also when inserted in the electron microscope. Because of this condition, we need to use a cryospecimen holder. As explained before, in order to transfer the vitrified sample into the cryospecimen holder, a specialized workstation is necessary. The workstation is cooled using liquid nitrogen. During the electron tomography experiment, the vitrified specimen needs to be kept cool. The temperature of the specimen in the holder is affected by the cooling of the liquid nitrogen inside the Dewar flask and the heating from the surrounding environment. The heating is opposed by the cooling of the Dewar flask filled with liquid nitrogen *(Dubochet, 1988)*.

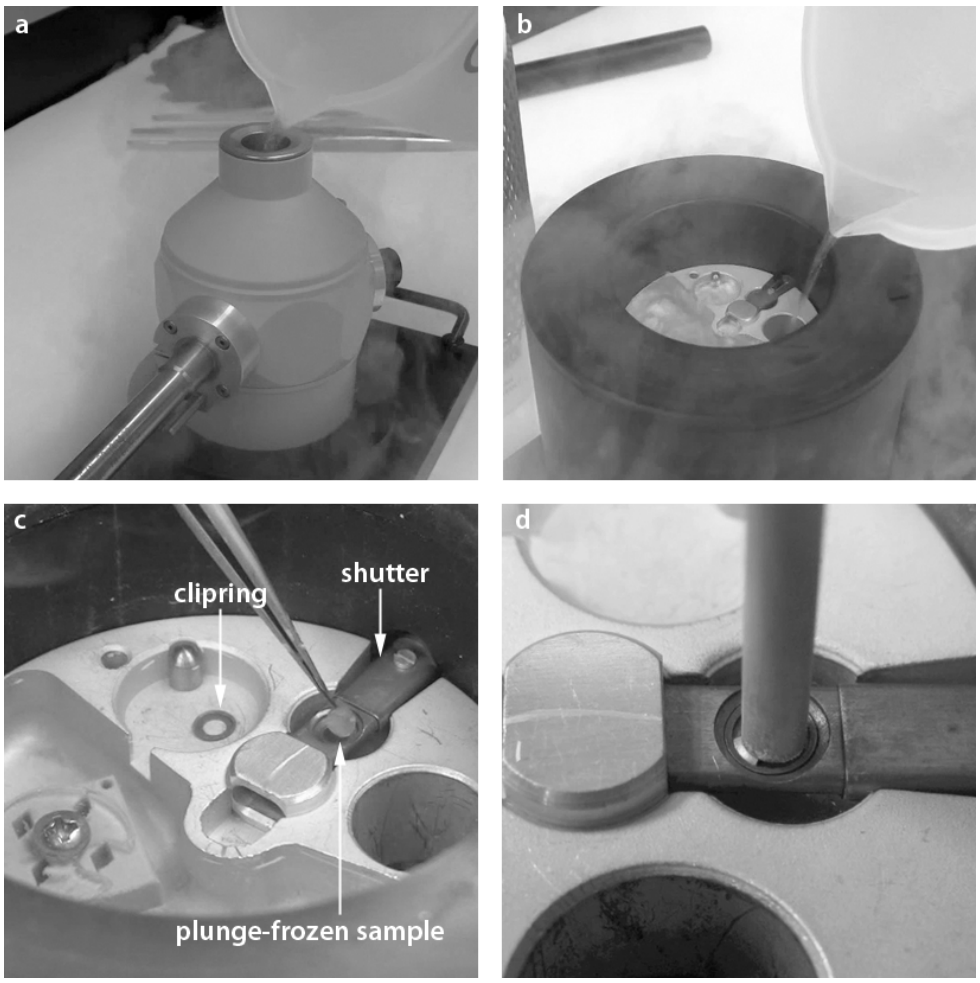

Figure 2.7: Cryotransfer: (a), (b) Pre-cooling of the cryospecimen holder and the workstation with liquid nitrogen. (c) Mounting the plunge-frozen sample. (d) The mounted, vitrified sample is secured with the clipring.

2.2.4 Cryogenic electron tomography for nano-assemblies

Imaging the vitrified sample

When switching from air dried samples to vitrified samples, we can no longer use the HAADF-STEM imaging technique. Due to the limited spacing in between the pole pieces of the Tecnai, which is equipped with a HAADF-STEM detector, we are not able to use the cryotransfer holder on the microscope. Therefore, the low dose TEM technique is applied using a Tecnai Spirit (FEI Company), where the images are recorded at 120kV. Figure 2.8 shows BF-TEM images of assemblies of both specimen, using the low dose set-up. The BF series of the assembly of nanospheres is acquired over $\pm 70°$ with increments of $2°$ and for the assembly of nanodumbbells,

we have acquired the series over ±64° with increments of 2°. The arrangement of the nanodumbbells appears to have a 3D structure.

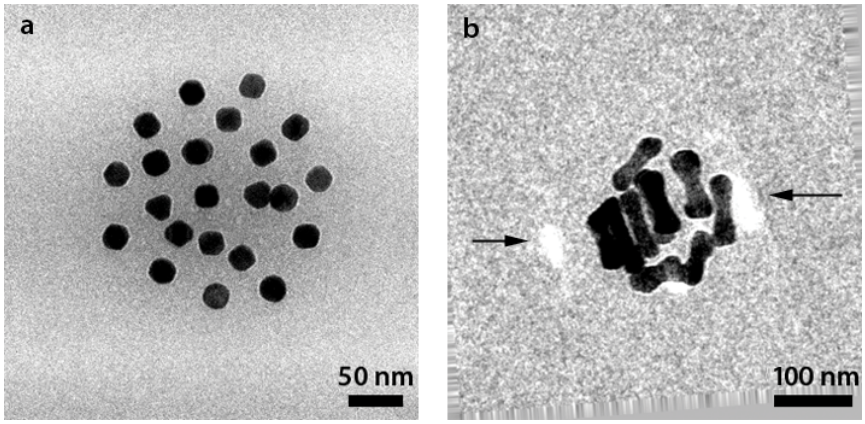

Figure 2.8: BF-TEM images of (a) an assembly of spherical Au nanoparticles and (b) of Au dumbbells in the vitrified sample. The displaced diffracted images are indicated with arrows.

Results

Here, we present some 3D visualizations of the reconstructions of nano-assemblies of the vitrified sample. These 3D visualizations, made in Amira, contain 3D structured assemblies, that confirm the maintenance of the initial structure when plunge-freezing the samples. In figure 2.9, we can clearly distinguish a 3D structured nano-assembly of Au dumbbells. For the nanospheres, a disk-like structure was found rather than

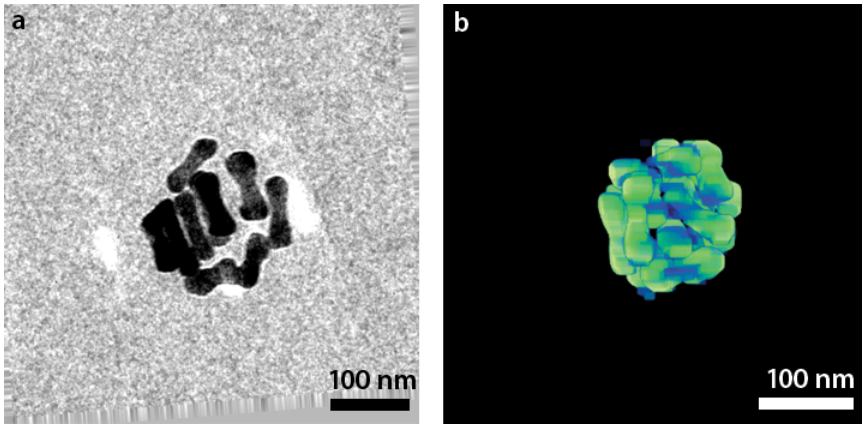

Figure 2.9: (a) A low dose BF-TEM projection image of an Au dumbbell assembly found in the vitrified sample and (b) its 3D reconstruction.

a planar structure (figure 2.10). There was no spherical assembly found, but the

disk structure is an indication of the presence and preservation of 3D structured assemblies. Based on these visualizations, we can conclude that plunge-freezing

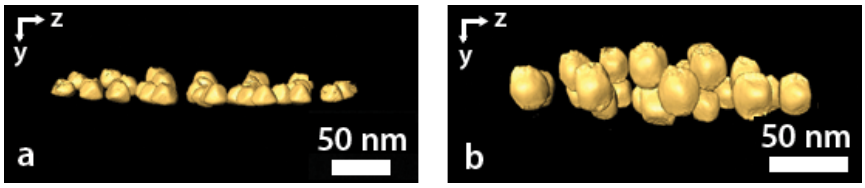

Figure 2.10: A 3D reconstruction of an Au nanosphere assembly found (a) in the air dried sample and (b) in the vitrified sample.

the nano-assembly samples is more promising than air-drying the samples. The assemblies are not collapsed on the support grid, because they are embedded in a thin layer of ice.

Discussion

In TEM mode, the contrast of amorphous structures is dominated by mass-thickness contrast and for crystalline structures, the contrast will depend almost entirely upon the diffraction contrast. For a combination of these structures, the TEM mode is less applicable because the projection requirement is not statisfied due to the diffraction contrast. The diffraction contrast is dependent on the orientation of the sample in relation to the electron beam and this will have no monotonic relationship with the amount of material through which the beam passes. Metallic structures have a crystalline structure and most biological and polymeric materials are amorphous. Thus, the investigated polymer-coated Au nanoparticles are a combination of both types of structures and therefore TEM tomography is not advisable to investigate these nano-assemblies. In figure 2.8b, the diffraction contrast is indicated with black arrows.
Although the polymer is not destroyed when plunge-freezing the sample, the technique is still not optimal for the investigation of nano-assemblies due to the diffraction contrast. In order to eliminate this problem, we need to investigate the assemblies with STEM tomography. Therefore, the vitrified samples are freeze-dried, which allows us to investigate the sample again at room temperature and acquire HAADF-STEM projection images.

2.3 Optimization of imaging mode

2.3.1 Freeze-drying procedure

In order to investigate the samples with HAADF-STEM, the vitrified sample is slowly heated. Then, the samples can be investigated at room temperature. The heating procedure is done using an environmental scanning electron microscope (ESEM), which is equipped with a Peltier stage. In a SEM, a fine beam of electrons scans onto a specimen surface. The electrons, which interact with the specimen surface layer, are detected and contain information about the surface of the specimen. A SEM must have a high vacuum region at the electron gun in order to generate and focus the electron beam. In a conventional SEM, the specimen chamber is at the same high vacuum level. In an ESEM, these two regions are seperated by at least two small pressure limiting apertures and can be kept at a different pressure (figure 2.11). In principle, an ESEM has a high pressure and gaseous specimen chamber and a high vacuum optics region. Due to the possibility of working at high pressure in the specimen chamber, hydrated specimen can be investigated and the specimen preparation necessary for the investigation using a conventional SEM is not required *(Ivarsson, 2012)*. The heating procedure using the ESEM is based on the opportunity of working at any pressure from vacuum up to one atmosphere.

- The temperature of the Peltier stage is set to 263K.
- The vitrified sample is transfered from a vessel filled with liquid nitrogen to the Peltier stage and immediately after inserting the sample, the chamber is pumped to low vacuum. This is necessary to establish a transition from the solid phase to the gaseous phase. In order to maintain the structure of the specimen, there cannot be a transition to the liquid phase.
- The heating procedure is started after several minutes, when the liquid nitrogen is evaporated. We wait until the specimen has the same temperature as the Peltier stage. The Peltier stage is heated up to 323K.
- After heating up the specimen, the chamber is brought back to atmospheric pressure.

The procedure is schematically shown in figure 2.12, where it is clear there is no transistion to the liquid phase involved in the heating procedure. It can therefore be expected that this heating technique will preserve the structures in the vitrified sample.

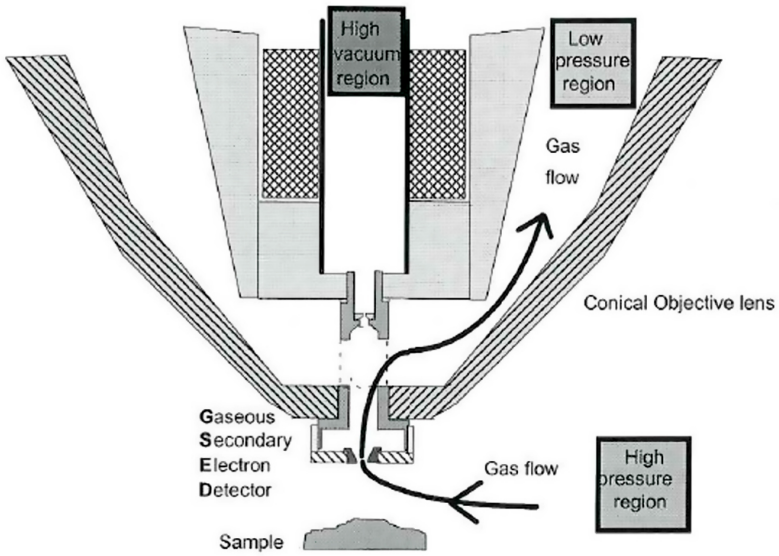

Figure 2.11: Schematic overview of an ESEM *(Ivarsson, 2012)*.

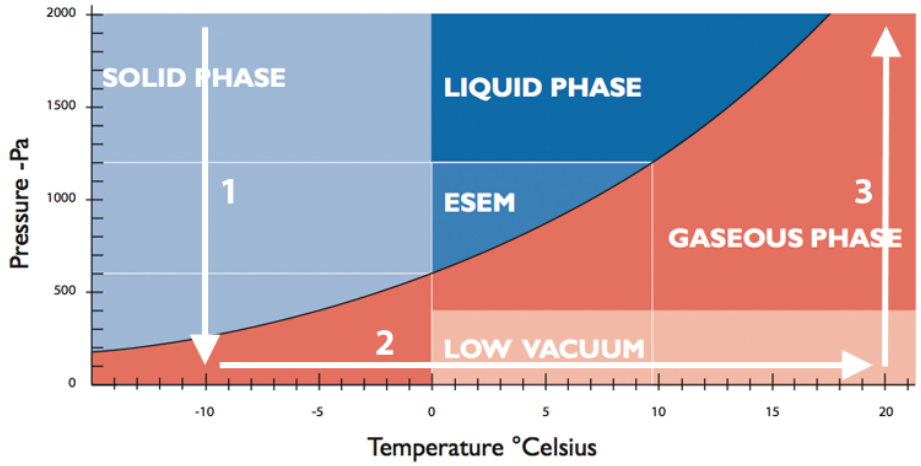

Figure 2.12: Phase diagram: (1) We pump the chamber to low vacuum. (2) The Peltier stage is heated up. (3) The atmospheric pressure is restored in the specimen chamber. The heating procedure does not contain a transition to the liquid phase.

2.3.2 Imaging the freeze-dried samples

The freeze-dried samples are investigated at normal TEM conditions and thereby we do not need the specialized cryotransfer holder, which was used to investigate the vitrified samples. Using the single-tilt holder (Fishione 2020), the microscope equipped with a HAADF-STEM detector can be used, which allows us to perform

STEM tomography. Imaging the nano-assemblies with the STEM imaging mode, fulfills the projection requirement because the diffraction contrast will not contribute to the image formation. Thereby, the freeze-dried samples are more attractive for electron tomography studies, when investigating nano-assemblies. Figure 2.13 shows HAADF-STEM images of nano-assemblies of both specimen in the freeze-dried sample.

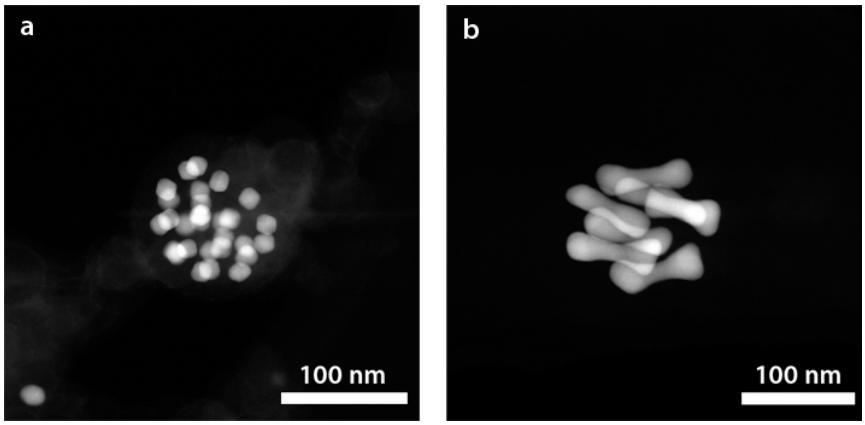

Figure 2.13: HAADF-STEM images of (a) spherical Au nanoparticles and (b) Au nanodumbbells, freeze-dried after vitrification.

It is of course also possible to acquire BF-TEM images of the freeze-dried samples. Because the nanoparticles are not so beam sensitive, it is not necessary to use the low dose mode. In figure 2.14 a BF-TEM image of a freeze-dried nano-assembly is shown.

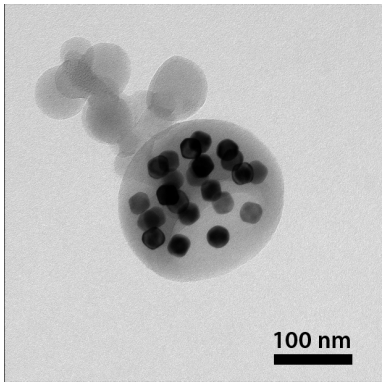

Figure 2.14: A BF-TEM image of a Au nanoparticle assembly found in a freeze-dried sample.

2.3.3 Results

The motivation to prepare, from the vitrified samples, the freeze-dried samples is the elimination of diffraction contrast and the simplification of the experiment, which can be performed at room temperature. Here, we present 3D visualizations which confirm the preservation of the 3D structure after slowly heating up the vitrified samples.

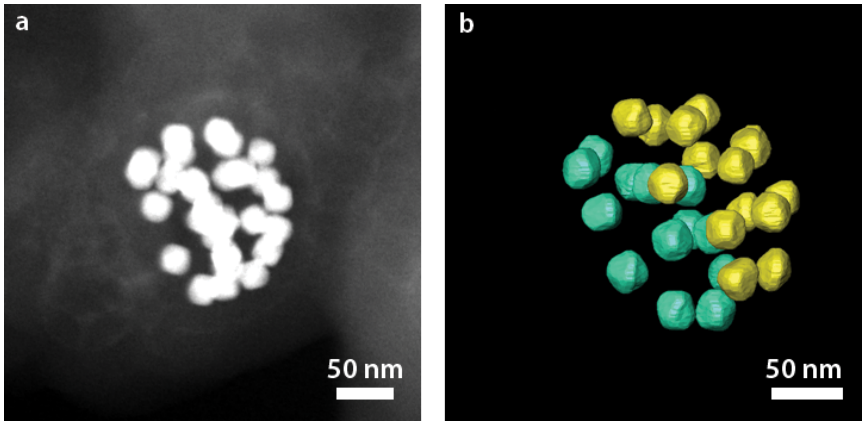

Figure 2.15: (a) A HAADF-STEM projection image of a nano-assembly of Au nanospheres, found in the freeze-dried sample and (b) its 3D reconstruction.

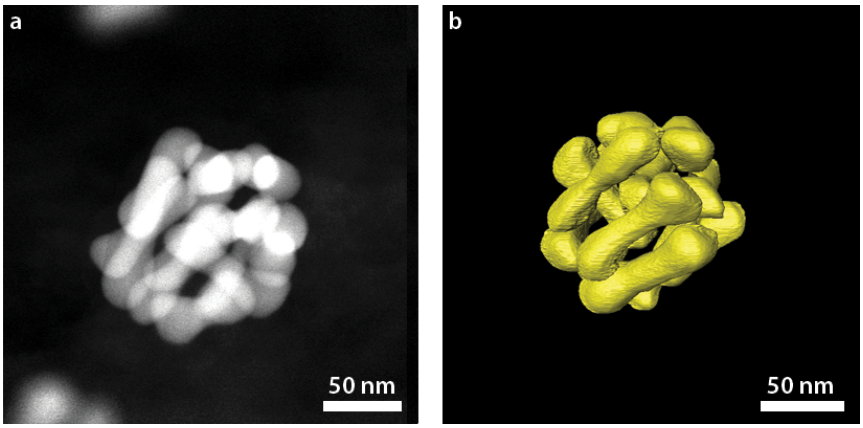

Figure 2.16: (a) A HAADF-STEM projection image of a nano-assembly of Au dumbbells, found in the freeze-dried sample and (b) its 3D reconstruction.

We conclude that freeze-drying is the optimized preparation method of TEM samples for the electron studies of nano-assemblies. In comparison to the vitrified samples, there is no need to work at low temperatures and the HAADF-STEM technique can be applied. Unlike the BF-TEM technique, HAADF-STEM does not suffer from diffraction artifacts.

Chapter 3

Optimization of the 3D reconstruction

After the alignment, all the acquired series are reconstructed based on a SIRT reconstruction algorithm implemented in FEI Inspect3D. However, for the BF-TEM series, we used the metal artifact reduction (MAR) algorithm to avoid the artifacts due to diffraction contrast in the BF-TEM projections, which appears as non-uniformities in the background of the reconstruction. For the tilt series aquired with HAADF-STEM, we performed the total variation minimization (TVM) algorithm.

3.1 Metal artifact reduction

Projection images with diffraction contrast in BF-TEM do not fulfill the projection requirement for TEM tomography since they lead to artifacts in the reconstructed background. We applied the metal artifact reduction (MAR) algorithm, in order to reconstruct the BF-TEM series with reduced background artifacts. This method is developed to apply on tilt series containing one or several particles with high atomic number (Z) embedded in a low Z matrix. Thereby, the investigation of polymer-coated Au nano-assemblies is suitable for the MAR method.
A threshold can be applied in the first reconstruction, so that only the bright region is reconstructed and the remaining regions are set to zero. Finding the optimal threshold is estimated by comparing the difference between the original sinogram and the sinogram of the tresholded reconstruction. In order to reconstruct the remaining regions, these sinograms are interpolated. This interpolated sinogram does no longer contain projection rays stemming from the bright particles, which contribute to the diffraction contrast. The bright particles will not be present in the reconstruction of the interpolated sinogram. The final result is established by combining the thresholded reconstruction, containing the bright particles, with the interpo-

lated reconstruction, containing the surrounding low Z matrix (figure 3.1). All the reconstructions are performed by a SIRT algorithm.

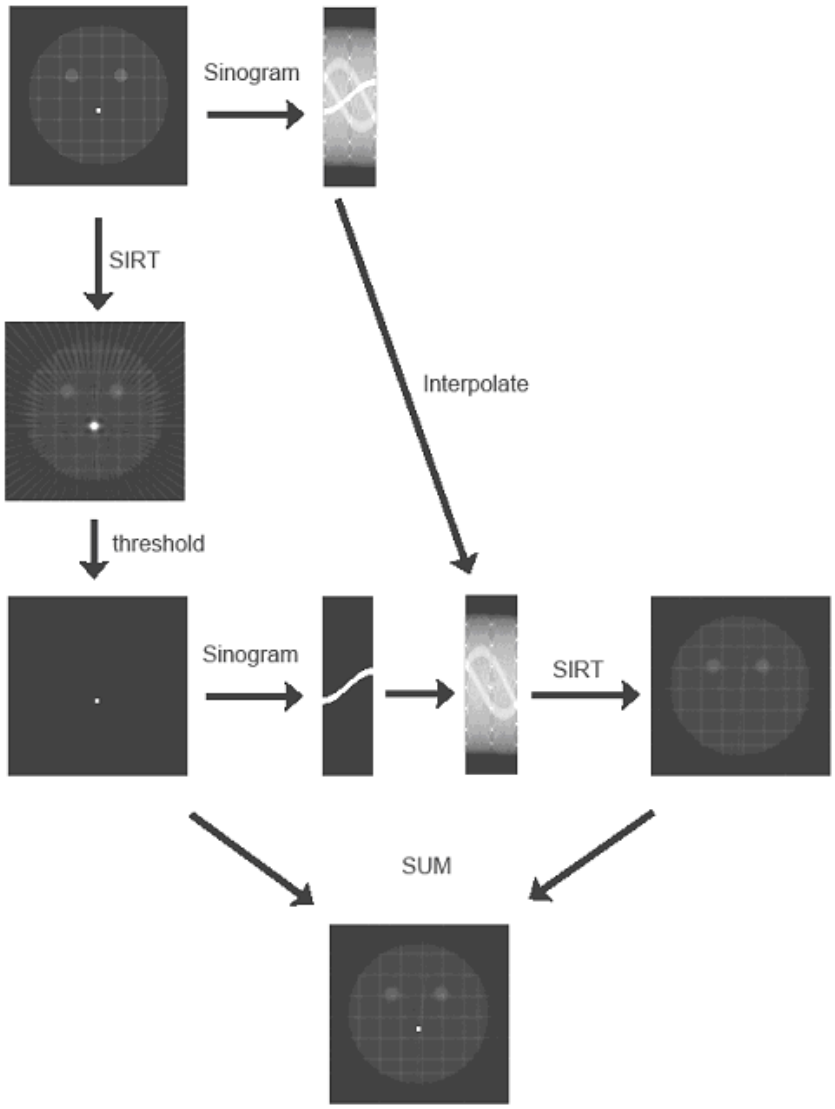

Figure 3.1: Schematic overview of the MAR algorithm.

3.1.1 MAR on nano-assemblies

In figure 3.2, a projection through the XY plane is given for both the SIRT reconstruction and the MAR reconstruction. The red box indicates the improvement of the reconstruction when using MAR. The MAR algorithm minimizes the background

artifacts by interpolating the background. We have to note that the intesity of the tilt series first is inverted, before calculating the reconstruction.

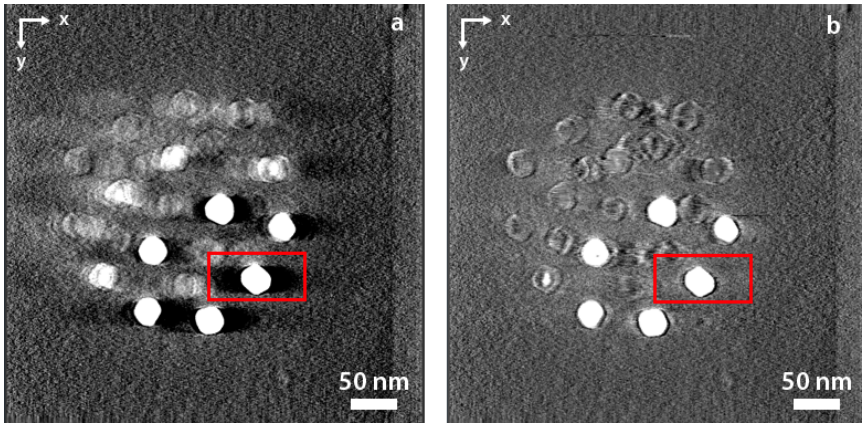

Figure 3.2: Orthoslices through the (a) SIRT reconstruction and (b) MAR reconstruction of a nano-assembly, corresponding to the XY plane. The tilt series are acquired with the low dose TEM mode, inverted and then reconstructed. The red box indicates the improvement when using MAR instead of SIRT.

A qualitative comparison between the MAR and the SIRT reconstruction reveals that reconstructions based on MAR result in a more uniform background by suppressing the artifacts. Therefore, we suggest to apply the MAR algorithm on the BF-TEM tilt series.

3.2 Total variation minimization

Both the WBP reconstruction, explained in section 1.3.1, and the SIRT reconstruction, explained in section 1.3.2, suffer from artifacts due to the missing wedge. The missing wedge artifacts are caused by the limited spacing between the pole pieces of the objective lens of the microscope and the tilt limit of the microscope goniometer, as mentioned before in section 1.3.2. However, iterative reconstruction techniques typically yield more accurate reconstructions than the analytical WBP technique. When an iterative technique is used to solve the reconstruction problem, we have to take into account the number of iterations. The correspondence between the calculated projections and the measured projection data improves at each iteration, however the noise may increase at each iteration. Therefore, we have to compromise between quality of the reconstruction and the signal-to-noise ratio (SNR). A recently developed iterative technique is total variation minimization (TVM) *(Goris, 2012)*. This new real space iterative reconstruction technique is based on the assumption that the reconstructed object has a sparse representation. The reconstructed image itself is not sparse, but the gradient of the object has only sharp grey value transitions

and is thereby sparse. In figure 3.3 a phantom object and its sparse representation are visualised.
The TVM algorithm tries to find the solution to the reconstruction problem $A\mathbf{x} = \mathbf{b}$ (in which A is the projection matrix, $\mathbf{x}$ the orignal object and $\mathbf{b}$ all the projection data, as mentioned above) with the lowest total variation. To accomplish the lowest total variation, the projection distance between the reconstructed object and the original projections and the total variation of the reconstructed object are simultaneously minimized.

$$\hat{x} = arg_x min\Big[TV(x) + \frac{\mu}{2}\| \, Ax - b \, \|_2^2\Big] \tag{3.1}$$

In equation 3.1, the total variation is computed as the norm of the discrete gradient of the reconstructed object and μ is a regularization parameter. A large value of μ leads to a result that resembles a SIRT reconstruction and will thereby introduce noise and missing wedge artifacts in the reconstruction as present in the SIRT reconstruction. When μ is chosen too small, the high frequency details of the reconstruction will be lost. The value of μ is chosen based on simulation studies. These simulations showed that $\mu = 0.5$ is considered as a good starting value *(Goris, 2012)*.
It was reported that the TVM algorithm is approximately four times slower than the SIRT algorithm, however the TVM reconstruction can be segmented in a more objective manner *(Goris, 2012)*. This is of great importance for quantitative measurements.

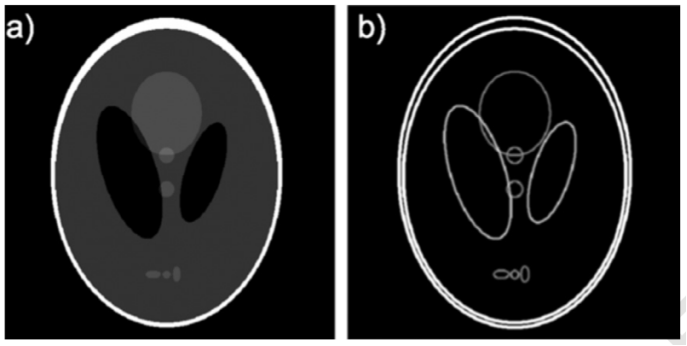

Figure 3.3: (a) Shepp Logan phantom object. (b) Gradient image of the Shepp Logan phantom object. It is clear that the gradient image is a sparse representation of the original object.

3.2.1 TVM on nano-assemblies

The TVM algorithm is initialy developed to apply on HAADF-STEM tilt series *(Goris, 2012)*. Here, we applied the algorithm on the BF-TEM tilt series as well.

Comparing the two orthoslices in figure 3.4, shows for both reconstructions, the presence of background artifacts. Although we applied the TVM on a low-dose BF-TEM series, the result did not yield a better result compared to a SIRT reconstruction. The low SNR and the presence of diffraction contrast might be the reason to deteriorate the quality of TVM on a BF-TEM series. The MAR algorithm is still the best choice for the reconstruction of low dose TEM series.

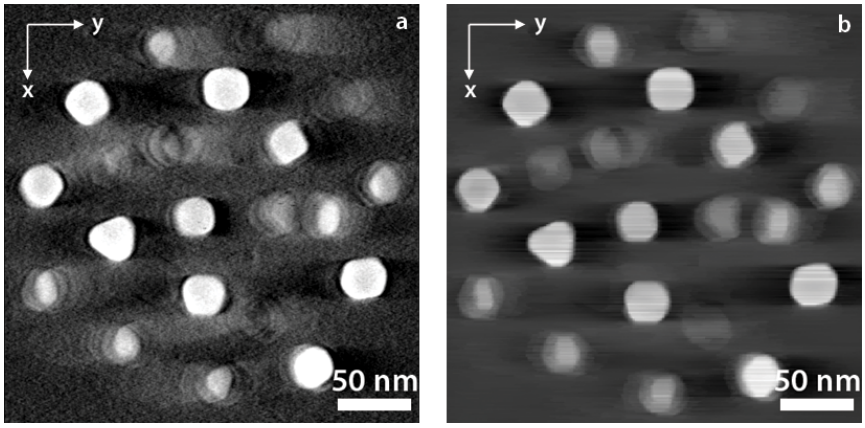

Figure 3.4: Orthoslices through (a) the SIRT reconstruction and (b) the TVM reconstruction, corresponding to the XY plane. The tilt series is acquired with the low dose TEM mode.

When the TVM algorithm is applied on HAADF-STEM tilt series, there is an improvement of the reconstruction. Figure 3.5 shows an orthoslice through the SIRT and TVM reconstruction corresponding to the XY plane, where we can clearly see that the background is more uniform in the TVM orthoslice. Also, the particle has a more defined shape, which will make segmentation easier in comparison when a SIRT reconstruction is used. In chapter 4, we try to compare the SIRT and TVM reconstructions quantitatively.

We can conclude, when optimizing the reconstruction of a BF-TEM tilt series, the MAR algorithm yields the best reconstruction. MAR obtains a more uniform background by interpolation. When the reconstruction of a HAADF-STEM tilt series needs to be optimized, we suggest the use of TVM.

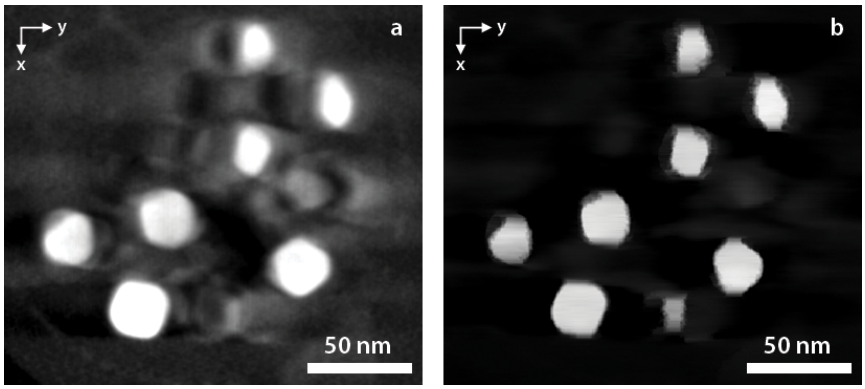

Figure 3.5: Orthoslices through (a) the SIRT reconstruction and (b) the TVM reconstruction, corresponding to the XY plane. The tilt series are acquired with the HAADF-STEM technique.

Chapter 4

Quantitative comparison

4.1 Comparison of different reconstruction techniques

The quality of a 3D reconstruction of an electron tomography experiment relies upon several experimental parameters, such as the maximum achievable tilt range, the number of 2D projections, the alignment of the acquired projections and of course the reconstruction algorithm. The limited spacing in between the pole pieces of the objective lens bounds the tilt range to a maximum tilt angle. The unsampled region in frequency space is commonly known as the missing wedge.
Due to the lack of projection images, the back projection reconstruction methods introduce significant artifacts to the reconstruction, which is why they are not applied in this work.
Other reconstruction algorithms which refine the reconstruction in an iterative way, suffer less in the presence of missing wedge artifacts than the back projection methods. A commonly used iterative reconstruction technique in tomography is called simultaneous iterative reconstruction technique (SIRT), which was discussed in detail in chapter 1.
We have applied SIRT and MAR for series acquired with BF-TEM and also SIRT and TVM for series acquired with HAADF-STEM. In order to compare the different reconstructions, the resolution of each tomogram is determined. It is however not straightforward to define resolution for a 3D reconstruction. In general, there are two main approaches for resolution determination in electron tomography; either methods performed in real space or in Fourier space. The real space methods are based on the point spread function (PSF) as a measure for the resolution and in Fourier space, frequency assessments are carried out *(Unser, 2005)*. In this work, we apply a real space method.

4.1.1 Determination of 3D resolution

The methodology to measure the resolution, is based on determination of the edge spread function (ESF), which is derived from an edge profile of a reconstructed particle *(Heidari Mezerji, 2011)*. The final 3D reconstruction is conceptualized by considering each point of the object to be convoluted by the PSF of the system. Therefore, approaches to determine the PSF will lead to a measurement of the resolution of the system. Particularly because of the missing wedge, the resolution will be anisotropic.
It is not straightforward to derive an analytic expression for a 3D-PSF of an electron tomography experiment, therefore the PSF is characterized by experimentally measuring its full-width at half-maximum (FWHM) along the three principal axes, which results in three 1D-PSFs. The X direction is perpendicular to the tilt axis and the electron optical axis, the Y direction represents the tilt axis and the Z direction the electron optical axis. A schematic drawing is presented in figure 4.1.

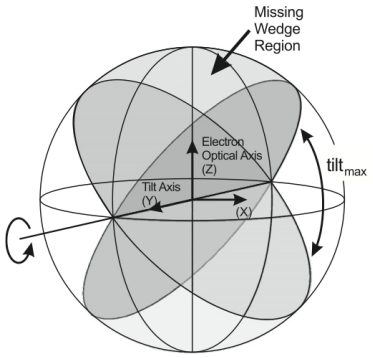

Figure 4.1: Schematic view of the geometry of a single tilt axis tomography experiment. The sample is placed at the origin *(Heidari Mezerji, 2011)*.

In systems containing individual, homogenous particles, according to the principles of HAADF-STEM imaging, the edge of a particle can ideally by represented by an edge step function, however in practice this edge is convolved with the 1D tensor of the PSF.
Therefore, by measuring the intensity profile along the edge of a particle and fitting to an analytical model of ESF, one would be able to derive the 1D-PSF. The ESF model is given by the following equation:

$$\mathrm{ESF}(x) = \frac{a_1}{1+\exp(\frac{r-x}{\sigma})} + \frac{a_2}{1+\exp(-\frac{r-x}{\sigma})} \tag{4.1}$$

The equation is fitted by a non-linear least squares method implemented in MATLAB. In this model, visualized in figure 4.2, a_1 is the intensity of the Au nanoparticle and a_2 the intensity of the background, thus $a_1 > a_2$. The parameter σ represents

the width of the step function. In order to determine the resolution, the model function (4.1) is derivated. The FWHM of the first derivative is used as estimate for the resolution in a certain direction (X, Y, Z), which is equal to 3.53σ.

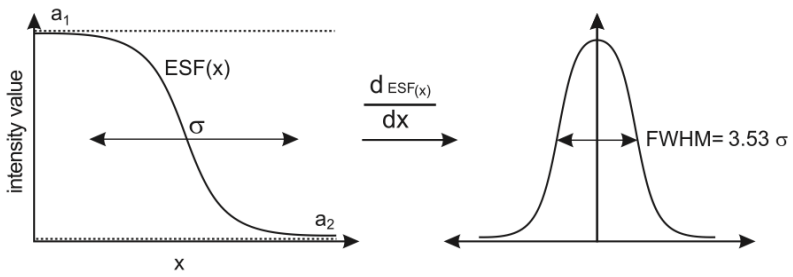

Figure 4.2: Schematic representation how to determine the resolution from the analytical function, where the FWHM of the first derivative of the ESF is used to determine the resolution *(Heidari Mezerji, 2011)*.

To obtain a relevant edge profile, particles with a clear edge perpendicular to a principal tomography axis are selected. The intensity profile is chosen symmetrically around the edge onset. Once these profiles are obtained, the parameter σ is estimated using a non-lineair least-square fitting in MATLAB. The procedure is schematically shown in figure 4.3. It should be noted that the approach as proposed in *(Heidari Mezerji, 2011)* was developed for HAADF-STEM tomography. The methodology is not applicable on BF-TEM series which suffer from background artifacts. These artifacts create a false background close to the particle, which will influence the resolution measurements drastically. An additional problem to the BF-TEM series, are the possible Fresnel fringes due to higher underfocus values. It is clear from figure 4.4, that the Fresnel fringes will interfere with the edge profile.

4.1.2 Results

As mentioned before, we believe that a nano-assembly of nanoparticles is suitable for the TVM algorithm, because of the well-defined shape of the particles. For the comparison between a SIRT reconstruction and a TVM reconstruction of HAADF-STEM tilt series, we can definitely use the proposed resolution measure. The results are presented in figure 4.5. For both cases the best resolution value is obtained along the tilt direction (Y) and it is deteriorated along X and Z (electron optical direction) respectively. The resolution along the electron optical axis (Z) is the worst due to the presence of the missing wedge. The lack of information at high tilt angles will appear as an elongation along the Z axis. The resolution values in X and Y are comparable for both SIRT and TVM. An improvement is observed in the Z direction, where the resolution of the SIRT reconstruction changes from 9.06 ± 0.40 to 5.37 ± 0.40 for the

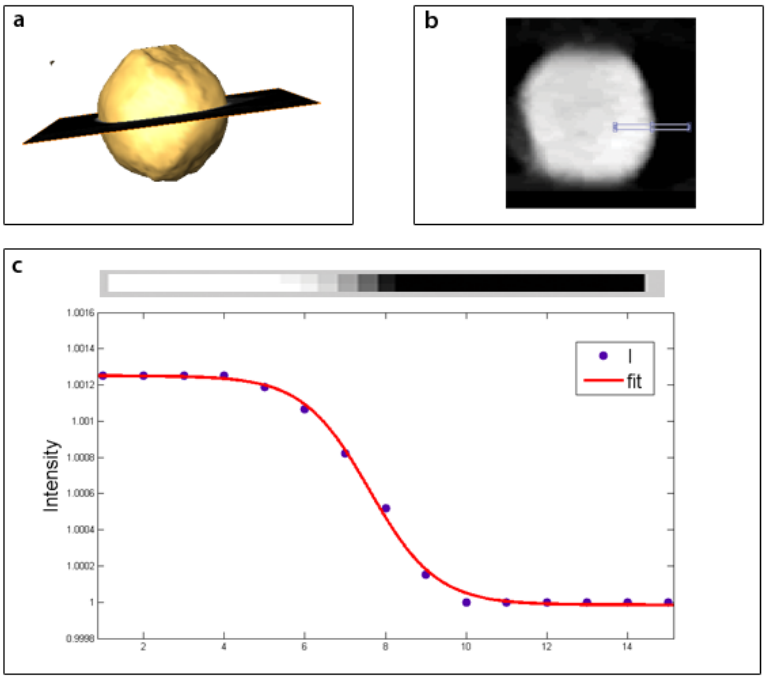

Figure 4.3: Determination of resolution in successive steps. (a) 3D reconstruction with the selection of an orthoslice with a relevant particle. (b) The edge profile is chosen in the orthoslice. (c) he edge profile intensities are fitted.

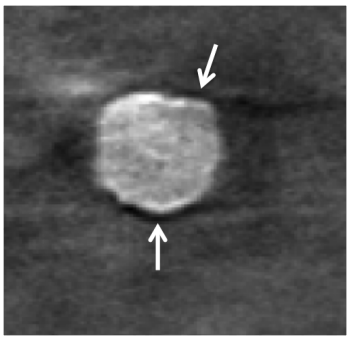

Figure 4.4: Orthoslice of a SIRT reconstuction of an acquired tilt series with higher underfocus. The white arrow indicate the Fresnel fringes.

TVM reconstruction. The resolution in Z direction is therefore improved by a factor of 40%. In general, the TVM algorithm will improve the resolution, especially along the Z direction. Thereby, TVM is a useful technique to reduce the missing wedge artifacs as stated before in the literature *(Goris, 2012)*. A TVM reconstruction is also easier to segment in comparison to the SIRT reconstruction, due to the sharper edges, which is convenient for the quantification of the nano-assemblies.

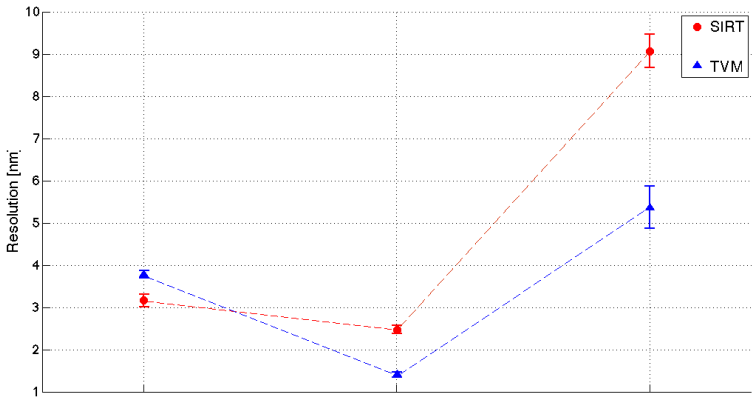

Figure 4.5: The resolution values acquire using 1D-PSF method from the HAADF-STEM series of Au nanodumbbell assemblies. The series are recorderd over a tilt range of $\pm 76^{\circ}$ with an increment of 2°.

Chapter 5

Conclusion

The aim of this work was to characterize nanoparticle assemblies in 3D in the most optimal electron tomography experiment. This optimization can be divided into three separate steps:

- the optimization of the preparation method
- the optimization of the imaging technique
- the optimization of the reconstruction algorithm

When depositing one or two droplets of suspension on the TEM support grid, the assemblies in the suspension have the tendency to collapse on the grid upon solvent evaporation and polymer desintegration. Therefore, the air dried samples cannot be used for the 3D investigation and characterization of nano-assemblies. The plunge-freezing method is therefore used to maintain the structure of the nano-assemblies. This preparation technique is initialy developed for the investigation of biological samples. In this work, it is demonstrated that the technique is also applicable to nano-assemblies. The initial structure of the assembly was successfully maintained. There is however a drawback since imaging a vitrified sample requires a low dose TEM mode. BF-TEM does not fulfill the projection requirement for electron tomography, due to the contribution of diffraction contrast during the image formation. The diffraction contrast will lead to artifacts. In order to eliminate the diffraction contrast, we propose to freeze dry the vitrified samples. This heating procedure does not involve a transition from the solid phase to the liquid phase, but directly goes to the gaseous phase, which maintains the 3D structure of the assemblies. A combination of these freeze-dried samples and the HAADF-STEM imaging technique is the optimized acquisition for the investigation of nano-assemblies.
In the next step, we tried to optimize the reconstruction of both the BF-TEM tilt series and the HAADF-STEM series. To minimize the background artifacts in the

BF-TEM reconstructions, we conclude that reconstructing the series with the metal artifact reduction (MAR) algorithm yields the best results. The optimal reconstruction algorithm for the optimized acquisition experiment, freeze dried samples in combination with HAADF-STEM imaging, is the total variation minimization (TVM) algorithm. The reconstuctions using TVM were compared to the simultaneous iterative reconstruction technique (SIRT) based on a resolution measure. We conclude that the optimized electron tomography experiment for the investigation of nano-assemblies is a combination of freeze-drying the samples, acquiring the tilt series with the HAADF-STEM imaging technique and reconstructing the tilt series with the TVM algorithm. The optimized protocol is illustrated in figure 5.1.

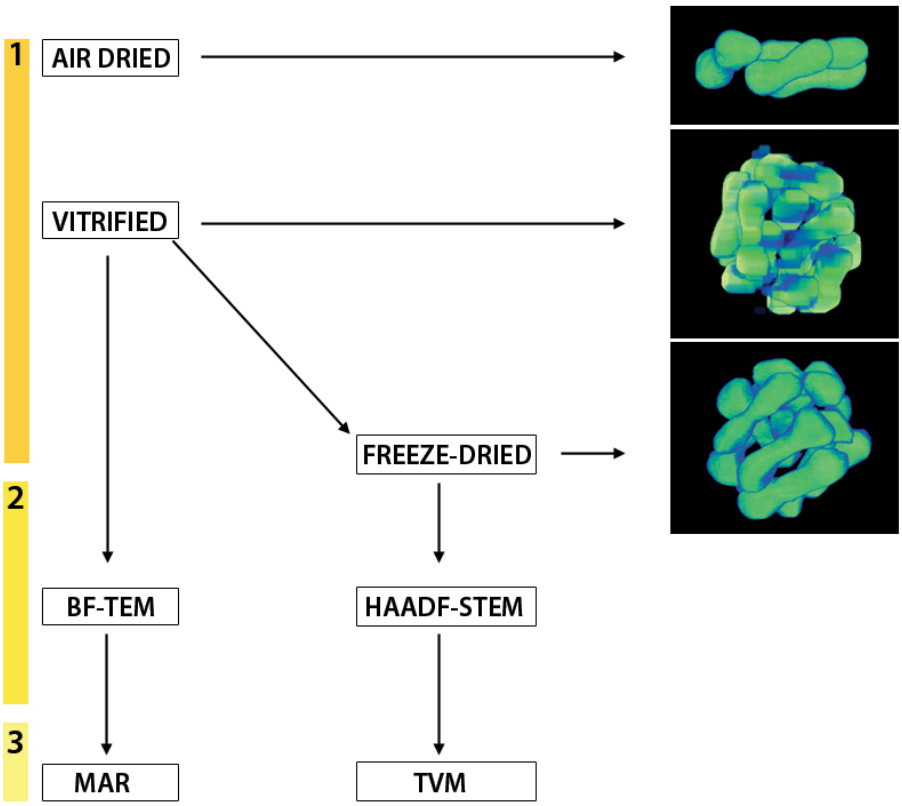

Figure 5.1: A schematic overview of the experimental study. (1) In order to characterize nano-assemblies, the structure of the assemblies should be preserved during the sample preparation. Air drying will alter the 3D structure and is thereby not applicable for the 3D characterization of material science samples. Plunge-freezing, yielding vitrified samples, and freeze-drying maintains the structure and thereby, they can be used for further investigation. (2) The vitrified samples are restricted to the use of BF-TEM imaging, which includes the contribution of diffraction contrast yielding artifacts. The freeze-dried samples can be studied using HAADF-STEM. (3) Finally, the reconstruction algorithm is optimized. MAR is used to reconstruct the low dose BF-TEM tilt series of the vitrified samples and TVM for the reconstruction of the HAADF-STEM tilt series of the freeze-dried samples.

Bibliography

[1] Altantzis T., Goris B., et al, *Quantitative structure determination of large three-dimensional nanoparticle assemblies*. Particle & Particle Systems Characterization 30 (2013) 84-88.

[2] Alvarez-Puebla R. A., Liz-Marzán L. M., *Traps and cages for universal SERS detection*. Chemical Society Reviews 41 (2012) 43-51.

[3] Bellare J., Davis H., et al, *Controlled environment vitrification system: an improved sample preparation technique*. Journal of Electron Microscopy Technique 10 (1988) 87-111.

[4] Besenius P., Heynen J., et al, *Paramagnetic self-assembled nanoparticles as supramolecular MRI contrast agents*. Contrast Media & Molecular Imaging 7 (2012) 356-361.

[5] Chen C.-H., Sarma L., et al, *Architecture of PdAu Bimetallic Nanoparticles in Sodium Bis(2- ethylhexyl)sulfosuccinate Reverse Micelles As Investigated by X-ray Absorption Spectroscopy*. ACS Nano 1 (2007) 114-125.

[6] Dubochet J., Adrian M., et al, *Cryo-electron microscopy of vitrified specimens*. Quarterly Review of Biophysics 21 (1988) 129-228.

[7] Friedrich H., Frederik P., et al, *Imaging of Self-Assembled Structures: Interpretation of TEM and Cryo-TEM Images*. Angewandte Chemie-International Edition 49 (2010) 7850-7858.

[8] Glotzer S., Solomon M., et al, *Anisotropy of building blocks and their assembly into complex structures*. Nature Materials 6 (2007) 557-562.

[9] Goris B., Van den Broek W., et al, *Electron tomography based on a total variation minimization reconstruction technique*. Ultramicroscopy 113 (2012) 120-130.

[10] Grzelczak M., Sánchez-Iglesias A., et al, *Steric Hindrance Induces crosslike Self-Assembly of Au Nanodumbbells*. Nano Letters 12 (2012) 12 4380-4384.

[11] Guerrero-Martínez A., Crzelczak M., et al, *Molecular Thinking for Nanoplasmonic Design*. ACS Nano 6 (2012) 3655-3662.

[12] Guerrero-Martínez A., Alonso-Gómez J. L., et al, *From individual to collective chirality in metal nanoparticles*. Nano Today 6 (2011) 381-400.

[13] Hawkes P.W., *The electron microscope as a structure projector, in: Frank J. (Ed.), Electron Tomography: Three-dimenstional Imaging with the Transmission Electron Microscope*. Plenum Press, New York, London (1992).

[14] Heidari Mezerji H., Van den Broek W., et al, *A practical method to determine the effective resolution in incoherent experimental electron tomography*. Ultramicroscopy 111 (2011) 330-336.

[15] Heidari Mezerji H., *Quantitative electron tomography of nanoparticles*. Ph.D. Thesis, University of Antwerp (2012).

[16] Iancu C., Tivol W., et al, *Electron cryotomography sample preparation using the Vitrobot*. Nature Protocols 1 (2006) 2813-2819.

[17] Ivarsson M, Holmström S., *Scanning electron microscopy: The use of ESEM in Geobiology (chapter 39)*. Ed: Kazmiruk V., InTech (2012).

[18] Kellenberger E., *The response of biological macromolecules and supremolecular structures to the physics of specimen cryopreparation*. Cryotechniques in Biological Electron Microscopy, Springer (1978), 35-63.

[19] Kim J., Lee J. E., et al, *Designed Fabrication of a Multifunctional Poly- mer Nanomedical Platform for Simultaneous Cancer- Targeted Imaging and Magnetically Guided Drug Delivery*. Advanced Materials 20 (2008) 478-483.

[20] Kirkland E., Loane R., et al, *Simulation of annular dark field stem images using a modified multislice method*. Ultramicroscopy 23 (1987) 77-96.

[21] Koster A., Bárcena M., *Cryotomography: Low-dose Automated Tomography of Frozen-hydrated Specimens*. Electron tomography, Springer (2006) 113-161.

[22] Li S.-J., Shi Y.-F., et al, *Electrostatic self-assembly for preparation of sulfonated graphene/gold nanoparticle hybrids and their application for hydrogen peroxide sensing*. Electrochimica Acta 85 (2010) 628-635.

[23] Liang G., Ronald J., et al, *Controlled self-assembling of gadolinium nanoparticles as smart molecular magnetic resonance imaging contrast agents*. Angewandte Chemie Internation Edition 50 (2011) 6283-6286.

[24] Linic S., Christopher P., et al, *Plasmonic-metal nanostructures for efficient conversion of solar to chemical energy*. Nature Materials 10 (2011) 911-921.

[25] Martínez A., Pérez-Juste J., et al, *Recent Progress on Silica Coating of Nanoparticles and Related Nanomaterials*. Advanced materials 22 (2010) 1182-1195.

[26] Midgley P. A., Weyland M., *3D electron microscopy in the physical sciences: the development of Z-contrast and EFTEM tomography*. Ultramicroscopy 96 (2003) 413-431.

[27] Midgley P. A. & Bals S., *Electron Tomography, in Handbook of Nanoscopy, Volume 12*. Eds: Van Tendeloo G., Van Dyck D. and Pennycook S. J., Wiley-VCH Verlag GmbH Co. KGaA (2012).

[28] Nie Z., Petukhova A., et al, *Properties and emerging applications of self-assembled structures made from inorganic nanoparticles*. Nature Nanotechnology 5 (2010) 15-25.

[29] Pennycook S., *Z-Contrast Transmission Electron-Microscopy - Direct Atomic Imaging of Materials*. Annular Review of Materials Science 22 (1992) 171-195.

[30] Pennycook S. J., Rafferty B., et al, *Z-contrast Imaging in an Aberration-corrected Scanning Transmission Electron Microscope*. Microscopy and Microanalysis 6 (2000) 343-352.

[31] Radon J., *Über die Bestimmung von Funktionen durch ihre Integralwerte lngs gewisser Mannigfaltigkeiten*. Ber. Verh. König Sächs. Ges. Wiss. Leipzig, Math. Phys. Kl., 69 (1917) 262267.

[32] Rosi N., Mirkin C., *Nanostructures in Biodiagnostics*. Chemical Reviews 105 (2005) 1547-1562.

[33] Sánchez-Iglesisas A., Grzelczak M., et al, *Hydrophobic Interactions Modulate Self-Assembly of Nanoparticles*. ACS Nano 6 (2012) 11059-11065.

[34] Sun Y., Wang Y., *Monitoring of Galvanic Replacement Reaction between Silver Nanowires and $HAuCl_4$ by In Situ Transmission X-ray Microscopy*. Nano Letters 11 (2011) 4386-4392.

[35] Tam J. O., Tam J. M., et al, *Biodegradable Near-Infrared Plasmonic Nanoclusters for Biomedical Applications*. Plasmonics in Biology and Medicine VII: Proceedings of SPIE-The International Society for Optical Engineering, 7577 (2010)

[36] Tam J. M., Tam J. O., *Controlled Assembly of Biodegradable Plasmonic Nanoclusters for Near-Infrared Imaging and Therapeutic Applications*. ACS Nano 4 (2010) 2178-2184.

[37] Unser M., et al, *Spectral signal-to-noise ratio and resolution assessment of 3D reconstructions*. Journal of Structural Biology 149 (2005) 243-255.

[38] Williams D., Carter C., *Transmission Electron Microscopy: A Textbook for Materials Science*. Springer (2009).

[39] Xin H., Zheng H., *In Situ Observation of Oscillatory Growth of Bismuth Nanoparticles*. Nano Letters 12 (2012) 1470-1474.

[40] Yuk J., Park J., et al, *High-Resolution EM of Colloidal Nanocrystal Growth Using Graphene Liquid Cells*. Science 336 (2012) 61-64.

[41] Zheng H., Smith R., et al, *Observation of Single Colloidal Platinum Nanocrystal Growth Trajectories*. Science 324 (2009) 1309-1312.

List of common abbreviations

2D	2-Dimensional
3D	3-Dimensional
ADF	Annular Dark Field
BF	Bright-Field
DF	Dark-Field
DMF	Dimethylformamide
ESF	Edge Spread function
FWHM	Full-Width at Half-Maximum
HAADF	High Angle Annular Dark Field
HR	High Resolution
MAR	Metal Artifact Reduction
PSF	Point Spread Function
STEM	Scanning Transmission Electron Microscopy
SIRT	Simultaneous Iterative Reconstruction Technique
SNR	Signal-to-Noise Ratio
TEM	Transmission Electron Microscopy
THF	Tetrahydrofuran
TVM	Total variation minimization
WBP	Weighted Back Projection